Tropical cyclones and associated environmental fields in CMIP6 models

Article

Accepted Version

Camargo, S. J., Tippett, M. K., Sobel, A. H., Lee, C.-Y., Fosu, B. and Hodges, K. I. ORCID: https://orcid.org/0000-0003-0894-229X (2025) Tropical cyclones and associated environmental fields in CMIP6 models. Journal of Climate, 38 (15). pp. 3877-3902. ISSN 1520-0442 doi: 10.1175/JCLI-D-24-0629.1 Available at https://centaur.reading.ac.uk/120038/

To link to this article DOI: http://dx.doi.org/10.1175/JCLI-D-24-0629.1

Publisher: American Meteorological Society

Tropical Cyclones and Associated Environmental Fields in CMIP6 models

Suzana J. Camargo[a,b] , Michael K. Tippett[c] , Adam H. Sobel[a,c] ,
Chia-Ying Lee[a] , Boniface Fosu[d] , and Kevin I. Hodges[e]

[a] *Lamont-Doherty Earth Observatory, Columbia University, Palisades, NY*

[b] *Columbia Climate School, Columbia University, New York, NY*

[c] *Department of Applied Physics and Applied Mathematics, Columbia University, New York, NY*

[d] *Department of Geosciences, Mississippi State University, Mississippi State, MS*

[e] *National Centre for Atmospheric Science and Department of Meteorology, University of Reading, Reading, United Kingdom*

Corresponding author: Suzana J. Camargo, suzana@ldeo.columbia.edu

ABSTRACT: The authors analyze the environmental fields associated with tropical cyclone (TC) activity in the Coupled Model Intercomparison Project Phase 6 (CMIP6) models, as well as the TC-like storms in those models. First, the model biases in the historical climatological means of chosen environmental fields are evaluated against the fifth generation of the European Centre for Medium-Range Weather Forecasting (ECMWF) atmospheric reanalysis (ERA5). Second, we show that the interannual variability of these fields is typically much smaller in models than in reanalysis. Applying a mean bias correction to these fields before calculating tropical cyclone genesis indices improves the variability of the modeled indices compared to those in reanalysis, as well as the means, due to the nonlinear dependence of the indices on these fields. The authors consider how these environmental fields change in the CMIP6 models, using three future scenarios separately as well as combining scenarios and times according to specific greenhouse warming levels. Multiple proxies for TC activity are considered and we show that the signs of the future changes are dependent on the choice of genesis index. The relationship between climate sensitivity and potential intensity change across the multi-model ensemble is examined. The statistics of the TC-like structures in the historical simulations are also examined, using the number of tropical cyclones (NTC) and accumulated cyclone energy (ACE) as diagnostics, including calculations of the percentage changes in NTC and ACE at the end of the 21C as compared with the 20C. Large decreases in both of these quantities are found in the highest emission scenario.

1. Introduction

Future projections of tropical cyclone activity have been explored and discussed numerous times in the literature over the last few decades (Knutson et al. 2010, 2020; Camargo and Wing 2016; Camargo et al. 2023). An intrinsic problem is that tropical cyclones (TCs) require high horizontal resolution to be well simulated in numerical models, especially in order to represent high-intensity storms. At the same time, large numbers of years, ensembles, scenarios, and models are required to represent the climate change signal and its uncertainties. These two objectives are difficult to satisfy simultaneously.

One common approach has been to compare historical and future TCs' characteristics (e.g., frequency, intensity, and duration) in standard global climate models (e.g., Camargo 2013; Tory et al. 2013; Chand et al. 2017; Bell et al. 2019; Feng et al. 2024). Due to these models' low resolutions, among other reasons, such as systematic biases associated with convection parametrization, the resulting TC climatologies are not very realistic, with simulated TCs weaker and larger than those observed being a particularly obvious bias (Camargo and Wing 2016; Camargo 2013; Shaevitz et al. 2014).

A second approach is to analyze model TCs in high-resolution climate models (25 - 50 km grid spacings), as was done recently in the HighResMIP project (Haarsma et al. 2016; Roberts et al. 2020a,b). These studies show improved representation of TCs with increased resolution, consistent with other studies (Zhao and Held 2012; Manganello et al. 2012; Wehner et al. 2014; Roberts et al. 2015; Vidale et al. 2021; Russotto et al. 2022; Moon et al. 2020, 2022), in particular TC intensity, though there remain biases in multiple aspects of TC activity, such as track characteristics and landfall locations. However, the computational cost of these high-resolution climate simulations limits the number of ensemble members, number of future scenarios, and simulation duration. While the representation of TCs in convection-permitting models such as those in Judt et al. (2021) (2.5 - 8km) are much more realistic than in models with lower resolution, these simulations are typically too short (a few years or months) to provide robust TC projections. Currently, these high-resolution simulations are too computationally expensive to be performed using multiple ensembles and for many years, however the situation is changing fast (Schär et al. 2020).

Another common approach is to downscale global climate models to basin-scale using high-resolution regional models (Knutson et al. 2013, 2022; Patricola et al. 2014, 2017; Fu et al. 2019).

Drawbacks to this approach include that it does not produce consistent global (i.e., multi-basin) TC projections and that it has issues at basin boundaries (Landman et al. 2005; Zick and Matyas 2015; Baudouin et al. 2019). Global climate models with variable-resolution grids avoid boundary issues (Zarzycki et al. 2014; Stansfield et al. 2020), but only TCs over the region of high resolution are well resolved.

An alternative methodology is to generate synthetic storms, either using statistical (Vickery 2005; Hall and Jewson 2007; Nakamura et al. 2015; Bloemendaal et al. 2020) or statistical-dynamical (Emanuel et al. 2006; Lee et al. 2018; Jing and Lin 2020; Lin et al. 2023b; Xu et al. 2024) models. One appealing feature of these models is the low computational cost and consequent large sample number of TCs that can be easily simulated, though a drawback is the limited representation of physical processes.

An approach that bypasses model TCs is to infer the projection of TC characteristics based on environmental proxies (genesis indices, potential intensity, ventilation index, etc.) for TC activity (e.g. Emanuel 1988; Emanuel and Nolan 2004; Emanuel 2010; Tang and Emanuel 2010, 2012). However, the behavior of TC proxies in projections sometimes disagrees with TC projections from high-resolution models (Camargo et al. 2014; Wehner et al. 2015). Furthermore, genesis indices are based on statistical relationships, derived from reanalysis data and TC "best track" data sets from the recent historical period, rather than physical theory. Good performance of a genesis index in a particular basin, period, or time scale, using reanalysis fields does not guarantee good performance in models or in future climates.

Finally, all approaches used to make TC projections are impacted, indirectly or directly, by model biases. One well-known issue in Coupled Model Intercomparison Project Phase 5 and 6 (CMIP5 and CMIP6) models is their failure to match the observed strengthening of the tropical Pacific sea surface temperature (SST) zonal gradient over the historical period, possibly a consequence of model bias (Seager et al. 2019). Given the important role of the El Niño-Southern Oscillation (ENSO) in modulating TC activity, and the similarity of sea surface temperature (SST) trend patterns to El Niño (in models) or La Niña (in observations) this disagreement with observations may be expected to have important consequences for TC projections (Sobel et al. 2023).

This manuscript addresses the following topics in a large number of CMIP6 models: (i) biases in environmental fields associated with TC activity; (ii) the relationship between model TCs and environmental fields; changes in (iii) TC-related environmental fields and (iv) model TC activity with anthropogenic climate change. Once we examine the climatological and interannual variability biases across the CMIP6 models, we show their impact on genesis indices and propose a bias correction to address this issue. Next, we analyze the main characteristics of the TCs in the CMIP6 models and how they relate to model resolution and environmental fields. The response of environmental fields and TCs to greenhouse gases forcing is then discussed, including the role of aerosols in the different future scenarios.

Section 2 describes the environmental fields and proxies considered. The models, datasets and methods used are given in Section 3. The historical simulations are analyzed in Section 4 and future simulations in Section 5. The conclusions are presented in Section 6.

2. Environmental Field Proxies

We analyze the biases in the spatial climatological patterns and interannual variability of key environmental variables associated with TCs, including potential intensity (PI), vertical wind shear (VSH), column relative humidity (CRH), and absolute vorticity at 850hPa.

Potential Intensity (PI) is the theoretical maximum intensity that a TC could reach under given environmental conditions (Emanuel 1988). PI computed from reanalysis data explains both observed TC intensity trends and interannual variability to some degree (Emanuel 2000; Wing et al. 2007, 2015). Since Emanuel (1987) first showed that PI is expected to increase with anthropogenic climate change, projections of PI have been extensively discussed in the literature, including in previous generations of CMIP models, such as CMIP3 (Vecchi and Soden 2007a,b), and CMIP5 (Camargo 2013). Here PI is calculated following the Bister and Emanuel (2002) algorithm.

Deep-layer vertical wind shear (VSH), the difference between horizontal winds at 200 and 850 hPa, influences TC genesis and intensification (e.g., Rios-Berrios et al. 2023, and references therein). Overall, strong VSH tends to weaken TCs, as the TC vortex becomes vertically tilted. However, this response is sensitive to other factors, such as winds at other levels and the presence of dry environmental air. Earlier VSH projections under anthropogenic climate change have been widely discussed in the literature (Vecchi and Soden 2007b; Camargo 2013), as have recent observed trends (Kossin 2017) and the impact of decadal variability on Atlantic VSH projections

(Ting et al. 2019). Here we will analyze only the VSH magnitude, defined as the magnitude of the vector difference of winds at 200 hPa and 850 hPa.

The absolute vorticity at 850 hPa is calculated by adding the planetary vorticity to the relative vorticity at 850 hPa. The column relative humidity (CRH) is the ratio between the column integrated water vapor and the saturated water vapor, and the saturation deficit (SD) is their difference. The saturated water vapor is calculated following Bretherton et al. (2004). We were not able to calculate CRH, SD, and indices that used these variables for a few models that did not provide column water vapor as one of model ouputs in the CMIP6 database.

We consider three genesis index formulations. The first is the Emanuel's genesis potential index(GPI Emanuel and Nolan 2004; Camargo et al. 2007), a function of absolute vorticity at 850 hPa, vertical wind shear, potential intensity, and relative humidity at 600 hPa. Emanuel (2010) introduced a new version of GPI in which the humidity variable is a non-dimensional parameter χ, a measure of the entropy deficit of the middle troposphere. To differentiate from the original GPI, we refer to this new version here as "GPI-Xi".

The tropical cyclone genesis index (TCGI) comes from a Poisson regression of TC numbers with four environmental fields, as described in Tippett et al. (2011) and modified in Camargo et al. (2014). Similarly to Lee et al. (2018) and Lee et al. (2020a), we consider two versions of the TCGI. The first uses as humidity variable CRH (TCGI-CRH), and the second uses SD as the humidity variable (TCGI-SD). As initially discussed in Camargo et al. (2014) for a single climate model (HiRAM) and further explored in Lee et al. (2018, 2020a, 2022, 2023); Sobel et al. (2021) for reanalysis and CMIP5 models downscaling, these two TCGI versions have almost indistinguishable behavior in the historical climate, but differ in future projections. In addition to CRH or SD, TCGI includes PI, VSH and a "clipped" vorticity (maximum absolute value of 3.7×10^{-5} 1/s), as described in Tippett et al. (2011). The TCGI coefficients here are based on the European Centre for Medium-Range Weather Forecasts (ECMWF) 5th generation global reanalysis (ERA5; Hersbach et al. (2020)) reanalysis fields are given in the Supplemental Material and are an update of the version used in Lee et al. (2018, 2020a), which was based on the ECMWF ERA-Interim reanalysis (Dee et al. 2011). Dirkes et al. (2023) compared the characteristics of TCGI with Poisson fits based on different reanalyses, as well as GPI. They found that the differences in the representation of large-scale environmental variables relevant for TC development do not explain the differences and spread in TC climatologies across reanalyses.

Another proxy used is the ventilation index (VI) developed by Tang and Emanuel, which is a function of VSH, PI and χ, obtained based solely on theoretical concepts and is associated with both tropical cyclogenesis and TC intensification (Tang and Emanuel 2010, 2012).

Since most genesis indices include the environmental variables listed above, environmental biases will be translated into biases in these genesis indices as well.

3. Data, Models and Methods

a. Data

The environmental fields are taken from ERA5 reanalysis (Hersbach et al. 2020), regridded to a $2^\circ \times 2^\circ$ grid for comparison with the CMIP6 model data.

The observed tropical cyclone data are from the International Best Track Archive for Climate Stewardship (IBTrACS), version 4 from USA centers, with data from the National Hurricane Center or the Joint Typhoon Warning Center for all basins (Kruk et al. 2010; Knapp et al. 2010; Schreck et al. 2014).

The monthly CMIP6 (Eyring et al. 2016) data output were used for the calculation of the environmental fields and the CMIP6 6-hourly data for tracking the models' TCs. The models included in our analysis are listed in Tables 1 and 2, with additional information on the ensembles for environmental fields and TC tracking provided on Supplementary Tables S1–S4.

b. Models - Environmental Fields

We focus here on 45 CMIP6 global climate models (Eyring et al. 2016). The CMIP6 historical simulations are forced by common datasets that are largerly based on the best estimates of observations in the period 1850–2014. We consider three future scenarios, or socio-economic pathways for the period 2015–2100: SSP2-4.5, SSP3-7.0, and SSP5-8.5 (O'Neill et al. 2016). These correspond to middle of the road, regional rivalry and high emission scenarios, respectively.

The 45 models were chosen based on the availability of their environmental fields and scenarios necessary for our analysis and are listed in Tables 1 and2, together with the number of ensemble members considered. Not all 45 models have all variables for all scenarios analyzed. Therefore, we

Number	Model	Resolution	Historical	SSP2-4.5	SSP3-7.0	SSP5-8.5	References
1	ACCESS-CM2★	$1.9° \times 1.3°$	3	3	3	5	Bi et al. (2020)
2	ACCESS-ESM1-5■	$1.9° \times 1.2°$	20	11	10	40	Ziehn et al. (2020)
3	AWI-CM-1-1-MR	$1.9° \times 1.9°$	5	1	5	1	Semmler et al. (2020)
4	BCC-CSM2-MR★	$1.1° \times 1.1°$	3	1	1	1	Wu et al. (2019)
5	CAMS-CSM1-0	$1.1° \times 1.1°$	3	2	2	2	Rong et al. (2018, 2021)
6	CanESM5△	$2.8° \times 2.8°$	65	50	50	50	Swart et al. (2019)
7	CanESM5-CanOE	$2.8° \times 2.8°$	3	3	3	3	Swart et al. (2019)
8	CAS-ESM2-0	$1.4° \times 1.4°$	4	2	1	2	Zhang et al. (2020)
9	CESM2	$1.3° \times 0.9°$	11	6	6	5	Danabasoglu et al. (2020)
10	CESM2-WACCM	$1.3° \times 0.9°$	3	5	3	5	Danabasoglu et al. (2020)
11	CIESM	$0.9° \times 0.9°$	3	1	—	1	Lin et al. (2020)
12	CMCC-CM2-SR5★	$1.25° \times 0.9°$	1	1	1	1	Lovato et al. (2022)
13	CMCC-ESM2★	$1.25° \times 0.9°$	1	1	1	1	Lovato et al. (2022)
14	CNRM-CM6-1	$1.4° \times 1.4°$	28	10	6	6	Voldoire et al. (2019)
15	CNRM-CM6-1-HR★	$0.5° \times 0.5°$	1	1	1	1	Voldoire et al. (2019)
16	CNRM-ESM2-1△	$1.4° \times 0.4°$	9	10	5	5	Séférian et al. (2019)
17	E3SM-1-1	$1.0° \times 1.0°$	1	—	—	1	Golaz et al. (2019)
18	EC-Earth3★	$0.5° \times 0.5°$	18	22	7	8	Döscher et al. (2022)
19	EC-Earth3-CC	$0.5° \times 0.5°$	1	1	—	1	Döscher et al. (2022)
20	EC-Earth3-Veg■	$0.5° \times 0.5°$	9	8	6	8	Döscher et al. (2022)
21	EC-Earth3-Veg-LR■	$0.7° \times 0.7°$	3	3	3	3	Döscher et al. (2022)
22	FGOALS-f3-L	$1.3° \times 1.0°$	3	1	1	1	He et al. (2019)
23	FGOALS-g3	$2.0° \times 2.3°$	6	4	5	4	Li et al. (2020)

TABLE 1. List of CMIP6 models (part 1) used in this manuscript, their nominal approximate grid resolutions in degrees (longitude $\times$ latitude) their assigned number in this manuscript and the number of ensembles used in each case. The specific ensembles and model centers are given in the Supplementary material. Models underlined have been selected for downscaling. Models with a ★ have had TCs tracked for the historical and SSP5-8.5 simulations, though not necessarily for all ensembles available for the environmental fields. Similarly, models marked with a ■ (△) are tracked only for the historical (SSP5-8.5) simulations.The models underlined have been selected for downscaling.

.

included models with all environmental fields available for the historical and SSP5-8.5 simulations, and this leads to the 45 models chosen. The exceptions are the variables CRH and SD, which could not be calculated for the FGOALS-f3-L or FIO-ESM2-0 models, as the column water vapor from these models was not available. Only 40 models and 36 models have the necessary data available

Number	Model	Resolution	Historical	SSP2-4.5	SSP3-7.0	SSP5-8.5	References
24	FIO-ESM-2-0	$1.3° \times 0.9°$	3	3	—	3	Bao et al. (2020)
25	GFDL-CM4■	$1.3° \times 1.0°$	1	1	—	1	Held et al. (2019)
26	GFDL-ESM4	$1.3° \times 1.0°$	3	1	1	1	Dunne et al. (2020)
27	GISS-E2-1-G★	$2.5° \times 2.0°$	47	20	18	11	Kelley et al. (2020); Miller et al. (2021)
28	GISS-E2-1-H	$2.5° \times 2.0°$	25	—	—	5	Kelley et al. (2020); Miller et al. (2021)
29	HadGEM3-GC31-LL■	$1.9° \times 1.25°$	5	4	—	4	Kuhlbrodt et al. (2018); Andrews et al. (2019)
30	HadGEM3-GC31-MM★	$0.8° \times 0.6°$	2	—	—	4	Kuhlbrodt et al. (2018); Andrews et al. (2019)
31	INM-CM4-8	$2.0° \times 1.5°$	1	1	1	1	Volodin et al. (2010)
32	INM-CM5-0	$2.0° \times 1.5°$	10	1	5	1	Volodin et al. (2017)
33	IPSL-CM6A-LR★	$2.5° \times 1.3°$	30	8	11	6	Boucher et al. (2020)
34	KACE-1-0-G	$1.9° \times 1.25°$	3	3	3	3	Lee et al. (2020b)
35	KIOST-ESM2-0★	$2.0° \times 2.0°$	1	—	—	1	Pak et al. (2021)
36	MIROC6★	$1.4° \times 1.4°$	50	3	3	50	Tatebe et al. (2019)
37	MIROC-ES2L★	$2.8° \times 2.8°$	30	30	10	10	Hajima et al. (2020)
38	MPI-ESM1-2-HR★	$0.9° \times 0.9°$	10	2	10	1	Müller et al. (2018); Gutjahr et al. (2019)
39	MPI-ESM1-2-LR★	$1.9° \times 1.9°$	10	10	10	10	Mauritsen et al. (2019)
40	MRI-ESM2-0★	$1.1° \times 1.1°$	6	2	5	6	Yukimoto et al. (2019)
41	NESM3★	$1.9° \times 1.9°$	5	2	—	2	Cao et al. (2018)
42	NorESM2-LM★	$2.0° \times 2.0°$	3	3	3	1	Seland et al. (2020)
43	NorESM2-MM★	$1.0° \times 1.0°$	2	2	1	1	Seland et al. (2020)
44	TaiESM1★	$1.25° \times 0.9°$	2	1	1	1	Wang et al. (2021)
45	UKESM1-0-LL★	$1.9° \times 1.3°$	18	5	10	5	Sellar et al. (2019)

TABLE 2. List of CMIP6 models (part 2) used in this manuscript, their nominal approximate grid resolutions in degrees (longitude $\times$ latitude), assigned number in this manuscript and the number of ensembles used in each case. The specific ensembles, and model centers are given in the Supplementary material. Models with a ★ have had TCs tracked for the historical and SSP5-8.5 simulations, though not necessarily for all ensembles available for the environmental fields. Similarly, models marked with a ■ (△) are tracked only for the historical (SSP5-8.5) simulations. The models underlined have been selected for downscaling.

.

for the SSP2-4.5 and SSP3-7.0 scenarios. The environmental fields for all models were regridded to a common grid of $2° \times 2°$ in longitude and latitude.

For each model and scenario, all ensemble members available are included in the model ensemble mean and spread. The specific ensembles used in the environmental analysis are given in the supplementary material, Tables S1 and S2. We have also analyzed the environmental fields from the historical simulations of additional seven models (Table S3), and these will be used in a few specific figures that include model TCs statistics, as discussed below.

c. Models - Tropical Cyclones

We also discuss the characteristics of models' TCs, which were tracked using TRACK (Hodges 1994; Hodges et al. 2017) for the historical and SSP5-8.5 simulations of a subset of models that have the necessary 6-hourly output variables. The models with TCs tracked are marked in Tables 1 and 2. The TCs were tracked in the historical simulations for the period 1950–2014 and in the SSP5-8.5 for the full period (2015–2100). To increase the sample size of model TCs in the historical simulations, we calculated and included the number of TCs (NTC), accumulated cyclone energy (ACE), and environmental fields from a few models that had the necessary fields to track TCs in the historical but not the SSP5-8.5 simulations (see Table S3). The full list of models and number of ensembles in which TCs were tracked are given in Table S4.

d. Methods

All maps below show the August to October (ASO) seasonal mean in the northern hemisphere and January to March (JFM) seasonal mean in the southern hemisphere. These choices are not optimal for all basins, as the peak season varies from basin to basin, but we judged them optimal for the global collection of all basins. The choice is particularly poor in the case of the North Indian Ocean, however, where TCs occur almost exclusively in the pre- and post- monsoon seasons.

In cases when the environmental variables are integrated spatially, the tropical region over oceans between 0–40°N is considered for the northern hemisphere and similarly 40°S–0 in the southern hemisphere.

When defining model biases the reference is the climatology of ERA5 reanalysis fields in the period 1981 - 2010. For instance, the climatology of the ERA5 reanalysis is subtracted from the ensemble mean climatology of each model and that difference is defined as the climatological bias.

One standard diagnostic to analyze model biases is the Taylor diagram (Taylor 2001), which concisely describes how well model spatial patterns compare with observations and other models using correlation, root-mean-square difference, and the ratio of their variances. We use Taylor diagrams to compare the climatological environmental fields of CMIP6 historical model simulations with each other and with ERA5 climatological fields.

Two standard diagnostics are used to characterize the TCs tracked in the climate models: the number of TCs (NTC), and the accumulated cyclone energy (ACE) (Bell et al. 2000). The latter is defined as the sum of the squares of the TCs' maximum sustained wind speeds every six hours, for snapshots in which they exceed 34kt. Both these quantities have been regularly used to characterize TC climatologies in observations and models (e.g., Camargo and Sobel 2005; Camargo et al. 2005; Camargo 2013; Shaevitz et al. 2014). We examine the relationships between the environmental fields and these two TC quantities (NTC and ACE) as was done in Camargo et al. (2020) for models and Dirkes et al. (2023) for reanalyses.

When exploring the differences in the environmental fields between the 20C and 21C, we focus on the last 30 years of each century i.e., the difference between the multi-model means in 1971–2000 and 2071–2100. We consider the three future scenarios SSP2-4.5, SSP3-7.0, and SSP5-8.5 separately. The multi-model mean in the historical simulation subtracted from each future scenario is calculated using the same models in the historical and each of the future scenarios.

We also examine how the differences between the 20C and 21C depend on the models chosen. In that case, we follow Hausfather et al. (2022), who examined the properties of the CMIP6 models and separated them in two groups, the models that are "too hot" and the ones that are "likely". The distinction between these two groups is based on the transient climate response (TCR) metric (Zelinka et al. 2020; Nijsse et al. 2020). A model with a TCR in the range of 1.4–2.2°C is considered likely, while one with a larger TCR is labeled "too hot". TCR is defined as the amount of global warming in the year in which atmospheric CO_2 concentrations have doubled after having increased steadily by 1% each year relative to the 1850–1899 baseline, based on global mean surface temperature for each model.

An alternative way to look at how the environmental fields change in the future is based on global warming level (GWL), which combines multiple future scenarios and takes into account that models have different climate sensitivities. This approach is widely used in the Intergovernmental Panel on Climate Change (IPCC) Sixth Assessment Report (Arias et al. 2021). The calculations here follow the procedure developed by Seneviratne and Hauser (2020) for each model and future scenario:

1. The global annual ensemble mean temperature is calculated (latitude weighted).
2. The historical and future scenario temperature data are concatenated.
3. The mean of the temperature in the period 1850–1900 is subtracted from the concatenated data.
4. The 20-year centered running mean temperature is calculated.
5. Find the first year in which the running mean exceeds the desired GWL, or “central year”.
6. The period for each GWL is defined as starting 10 years prior to the “central year” and ending 9 years after that year.

This calculation is performed for three GWLs: 1.5°C, 3.0°C and 4.0°C. Once the years for each GWL are defined, the multi-model mean change by GWL is obtained by subtracting the 19C climatology (1850–1900). Note that one model can contribute with more than one ensemble mean field data for each GWL (Seneviratne and Hauser 2020).

Time-series of the global mean temperature are also constructed for each model ensemble mean, for both historical and future scenarios, using the procedure described above. For each model, a polynomial fit is then obtained for the temperature time-series, for the concatenated historical and future scenario. The same procedure is used for the mean PI in each hemisphere (tropics) to explore the relationship between global warming and PI.

4. Results - Historical Simulations

a. Model Biases - Climatology

In this section we analyze the biases in key environmental variables typically associated with tropical cyclone activity. We first examine the spatial biases in the variables’ mean climatologies, then in their interannual variability.

Figure 1 shows the differences between the CMIP6 models’ PI climatologies and that of ERA5 reanalysis for the period 1981–2010. Many models show a negative bias in PI in the deep tropics and positive bias in more subtropical regions. There is a clear consistency in the model biases across model families. This consistency is particularly striking for the CNRM models (CNRM-CM6-1, CNRM-CM6-1-HR, and CNRM-ESM2-1) which have predominantly larger values of PI than does

ERA5 in both hemispheres, particularly the southern. The EC-Earth3 models (EC-Earth3, EC-Earth3-CC, EC-Earth3-Veg, EC-Earth3-Veg-L4) also have similar patterns in their biases, with a bimodal pattern in the North Pacific (positive close to the Equator, negative around 20°N), a negative bias in most of the North Atlantic, and a strong positive bias in the southern hemisphere. For pairs of models with different model resolutions, namely CNRM-CM6-1 and CNRM-CM6-1-HR; HadGEM3-GC31-LL and HadGEM3-GC31-MM, MPI-ESM1-2-LR and MPI-ESM1-2-HR; NorESM2-LM and NorESM2-MM, the patterns of the biases are extremely similar between the two model resolutions, indicating that higher model resolution without other changes in the model configuration does not necessarily lead to improvement.

The biases in the models' VSH climatologies as compared with ERA5 are shown in Fig. 2. Many models have too high values of VSH in the northern hemisphere, centered around 20°N, and too low values closer to the tropics, particularly over the Pacific Ocean. There is less consistency in the biases in the southern hemisphere. Again, we notice very similar patterns in models from the same family, e.g., CanESM5 and CanESM5-CanOE or INM-CM4-8 and INM-CM5-0. In some models the magnitudes of the VSH biases are quite large, reaching values of the order of 20 m/s in some regions that are important for TC intensification (e.g., CAS-ESM2-0, MIROC-ES2L, NESM3). While most models have low shear close to the Equatorial region, that is not the case for the CESM2 and CESM2-WACCM models.

Biases in the CRH are shown in Fig. 3. CRH values are typically too low in most models. Some models have high values of CRH in the southern hemisphere, in particular in the Southeast Pacific, a region which typically has very little TC activity. High values of CRH are also present in many models in the South Atlantic and in the South Indian Ocean close to Australia.

Fig. 4 shows the Taylor diagrams for PI (top left), VSH (top right), CRH (bottom left) and absolute vorticity at 850 hPa (bottom right) in the northern tropics (Equator to 40°N) in ASO. For all variables, the multi-model mean (MMM) has better skill than most individual models. The correlation coefficient between each model and ERA5 is shown in the blue azimuthal angle. The smallest range in correlations occurs for the vorticity, with values close to 0.95 for all models, while in the case of PI, they range from 0.9 to 0.55. The centered root-mean-square error, shown in the green circles as the distance from ERA5, also has the smallest spread for the vorticity, and the largest for PI, probably due to the fact that the PI calculation includes multiple environmental

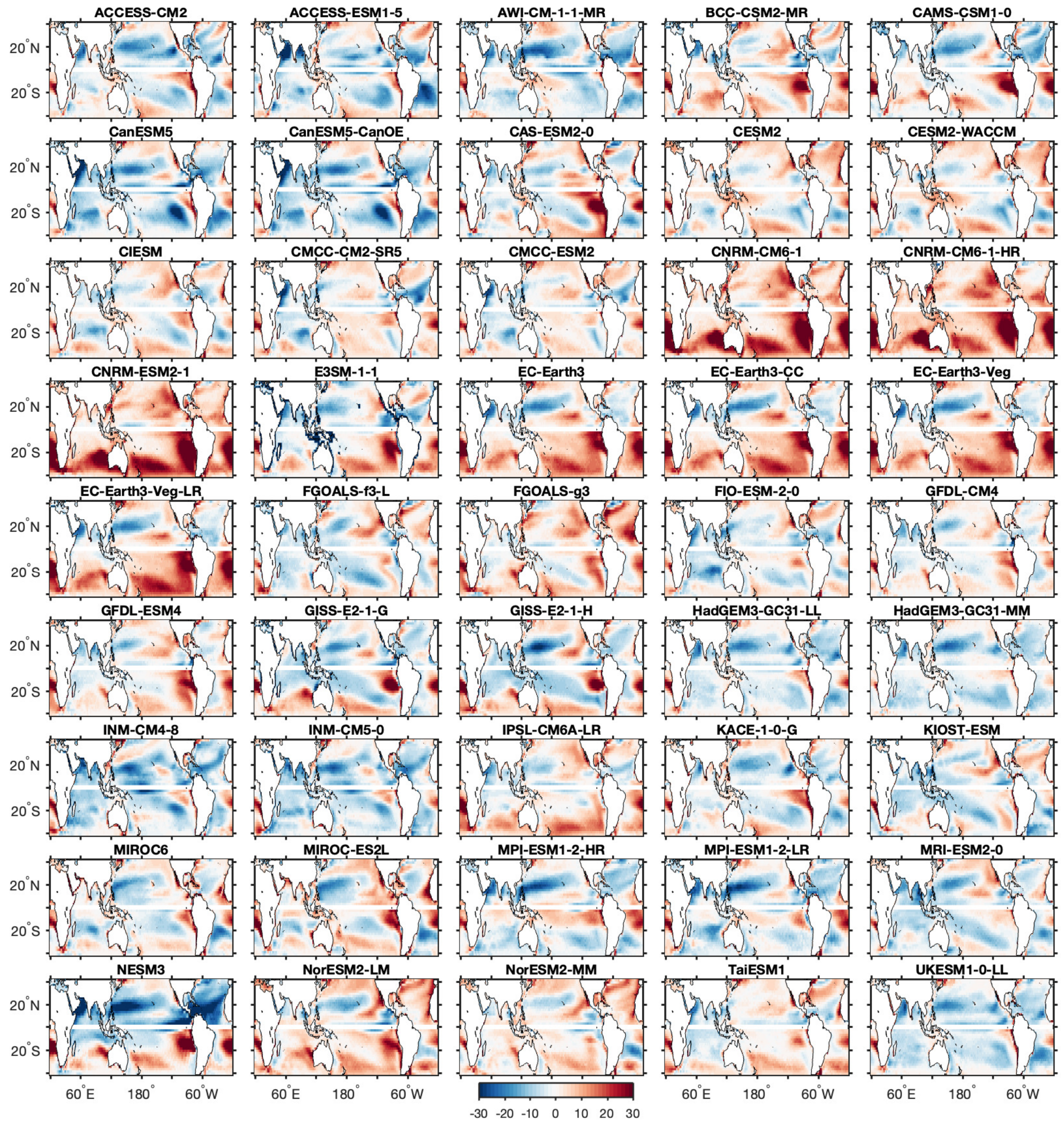

FIG. 1. Difference between the PI climatology (m/s) between CMIP6 models (ensemble mean) and ERA5 reanalysis for the period 1981–2010 for the August–October (ASO) season in the northern hemisphere and the January–March (JFM) season in the southern hemisphere.

variables. The standard deviation of the simulated pattern is given in the black circles. PI and VSH have a large spread across models, and vorticity has the smallest. Some model outliers have been identified by their numbers for PI and VSH. Models that are outliers in one variable are not

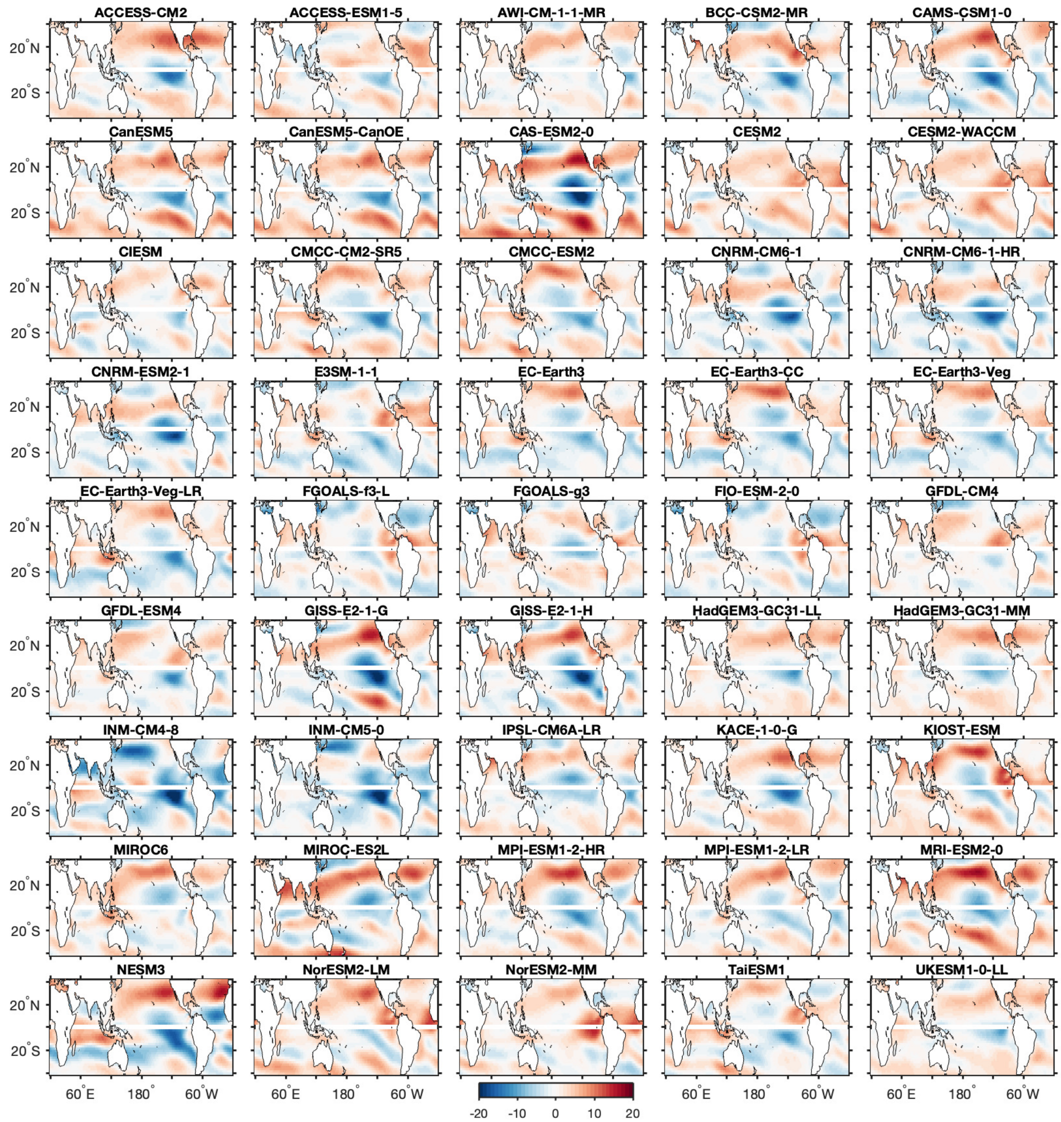

Fig. 2. Difference between the VSH climatology (m/s) between CMIP6 models (ensemble mean) and ERA5 reanalysis for the period 1981–2010, for ASO (JFM) in the northern (southern) hemisphere.

necessarily outliers in other variables, such that it would be inappropriate to identify the “best” or “worst” models overall using an individual Taylor diagram.

Interestingly, models tend to have higher correlation values and smaller root-mean square errors in the southern hemisphere tropics in JFM (not shown) when compared to the northern hemisphere tropics in ASO.

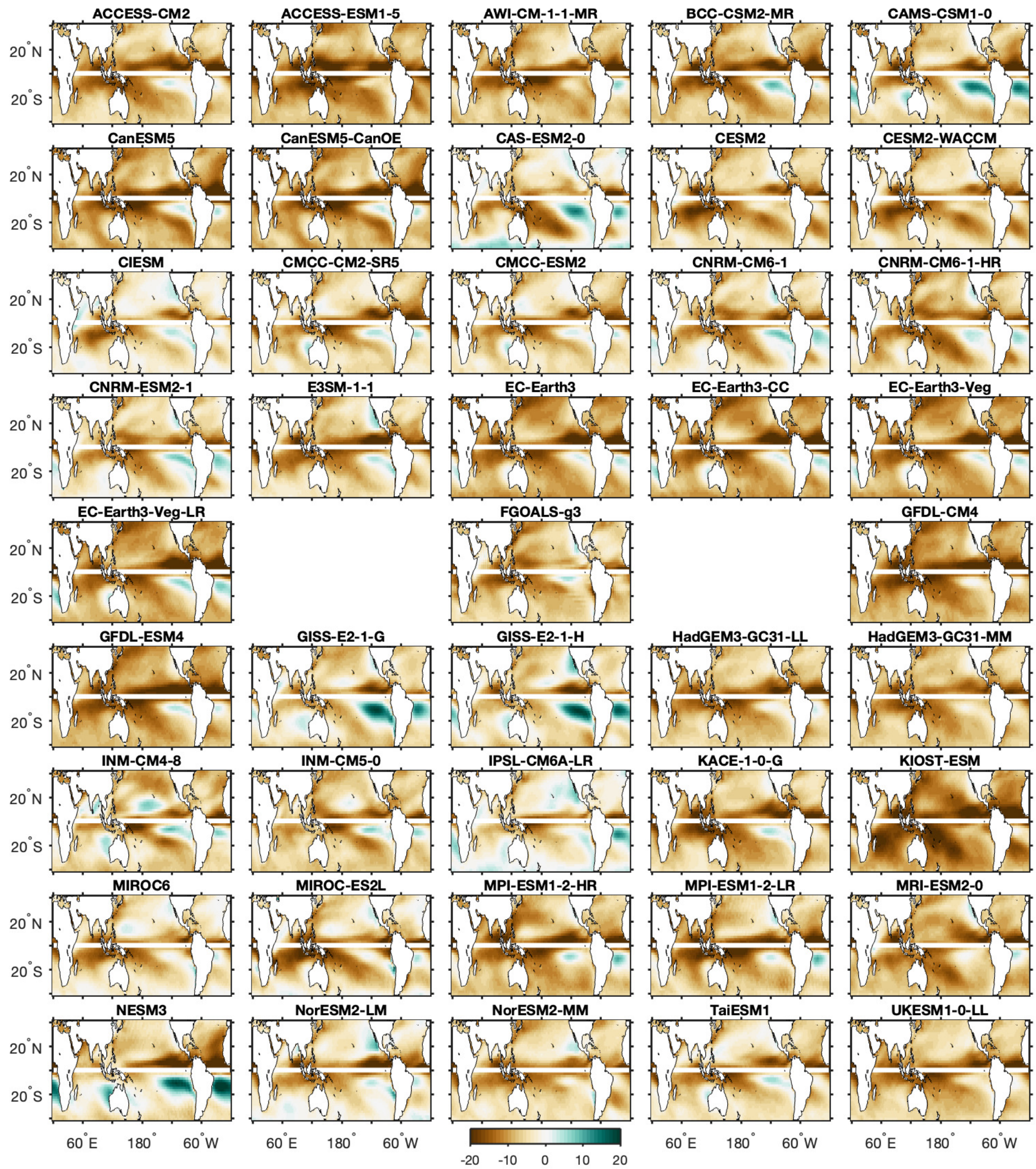

FIG. 3. Difference between the column relative humidity (CRH) climatology (in %) between CMIP6 models (ensemble mean) and ERA5 reanalysis for the period 1981–2010, for ASO (JFM) in the northern (southern) hemisphere. Models with missing variables to calculate CRH, SD and TCGI: FGOALS-f3-L and FIO-ESM-2-0.

b. Model Biases - Variability

Besides mean values, we examine how the models simulate the interannual variability of the environmental variables. We do this by examining the standard deviation (STD) of the seasonal

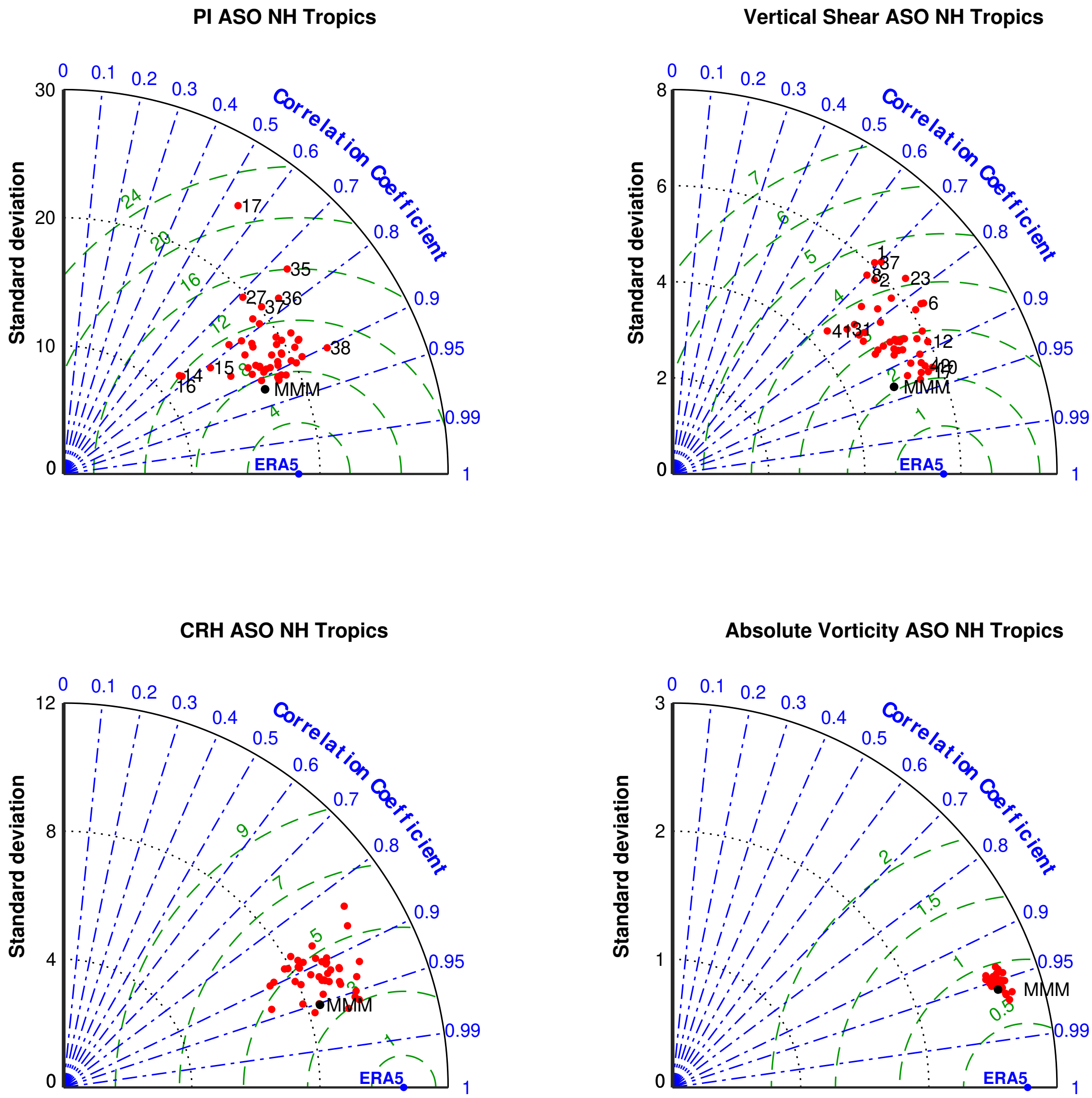

FIG. 4. Taylor diagram for the climatologies of PI (m/s), VSH (m/s), CRH (%) and absolute vorticity at 850 hPa (1/s)in the northern hemisphere tropics during ASO.

mean variables in each hemisphere for each model and compare that with the same quantity in the ERA5 reanalysis.

In Fig. 5 we show histograms of the standard deviation of the spatial mean of PI, VSH, CRH, and absolute vorticity in the northern hemisphere tropics during ASO for all models. For comparison, the ERA5 standard deviation for each variable is shown by the vertical red line. For all four variables the interannual variability in most models is much lower than is the case of ERA5. Only a few models have higher STD values than ERA5. In the case of PI, only EC-Earth3, for VSH: CAS-ESM2-0,EC-Earth3, GISS-E2-1-G, KIOST-ESM, for CRH: EC-Earth3 and GISS-E2-1-G and for vorticity: only CAS-ESM2-0, i.e. EC-Earth3 has high STD values for the 3 of the variables and GISS-E2-1-G and CAS-ESM2-0 for two of them. We also identify the models with lowest STD values in each case. The only models that have low STD values for three variables (VSH, CRH and vorticity) were INM-CM4-8 and INM-CM5-0, while CNRM-CM6-1-HR has low STD values for both CRH and vorticity. Similar behavior is noted in the southern hemisphere for the JFM season.

c. TCGI Bias Correction

One the consequences of the biases in the individual variables is that they lead to biases in proxies for TC activity that are functions of these variables. As an example, we show the impact of biases in the individual variables shown above on TCGI.

We calculate the spatially integrated annual mean TCGI in the historical simulations for a subset of 13 CMIP6 models and compare each with both the same quantity computed from ERA5 and the observed number of TCs (see Fig. 6 (a) and (c)). While there is a large spread in the magnitude of this bias across the 13 CMIP6 models, all of them have low values of integrated TCGI. This is true for both versions of the TCGI, TCGI-CRH-PI (Fig. 6 (a)) and TCGI-SD-PI (Fig. 6 (c)).

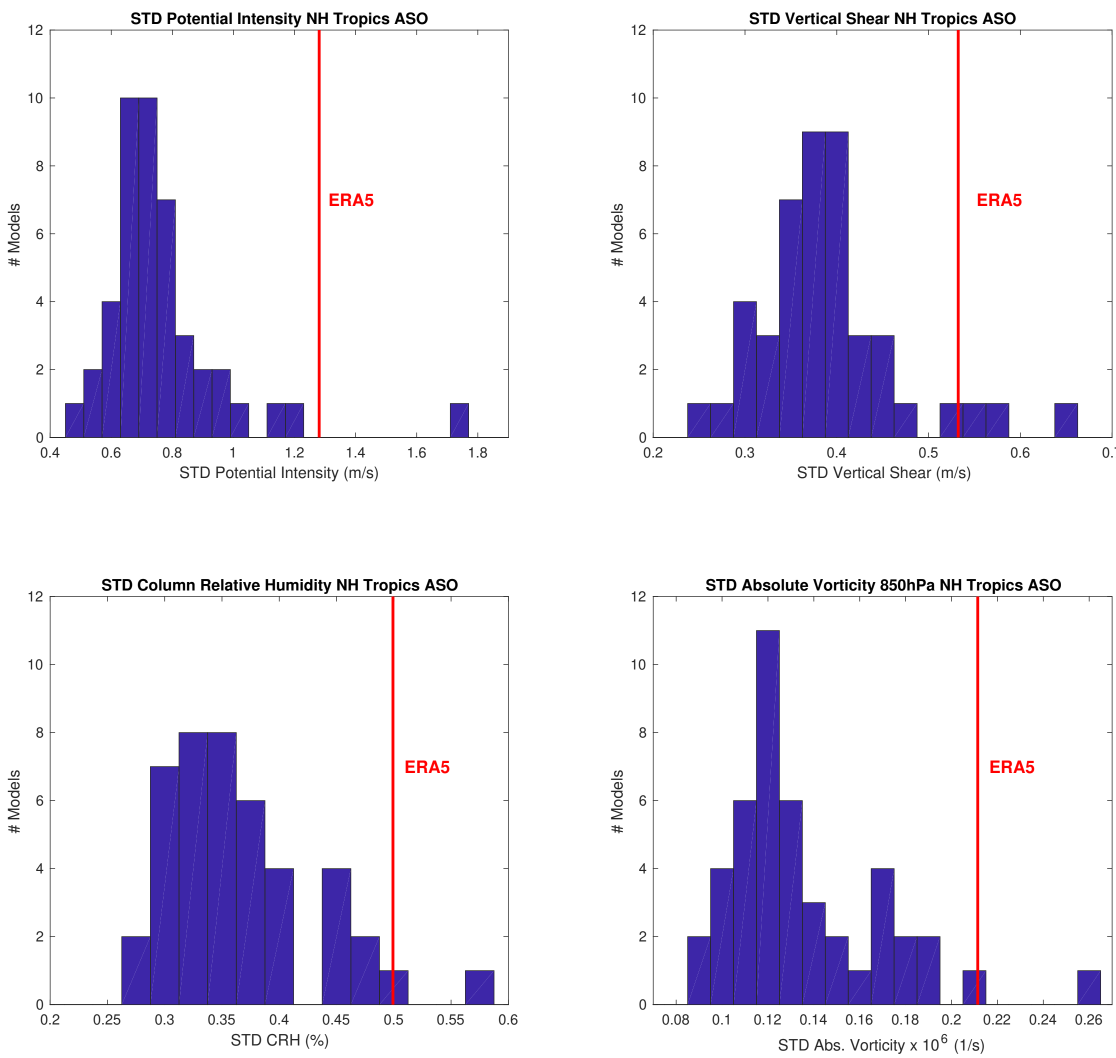

FIG. 5. Histograms of the standard deviation of interannual variability PI (m/s), VSH (m/s), CRH (%) and absolute vorticity at 850 hPa (1/s) climatology in the northern hemisphere tropics during ASO for CMIP6 models and ERA5 in the period 1950-2014. All ensembles available were considered for the models.

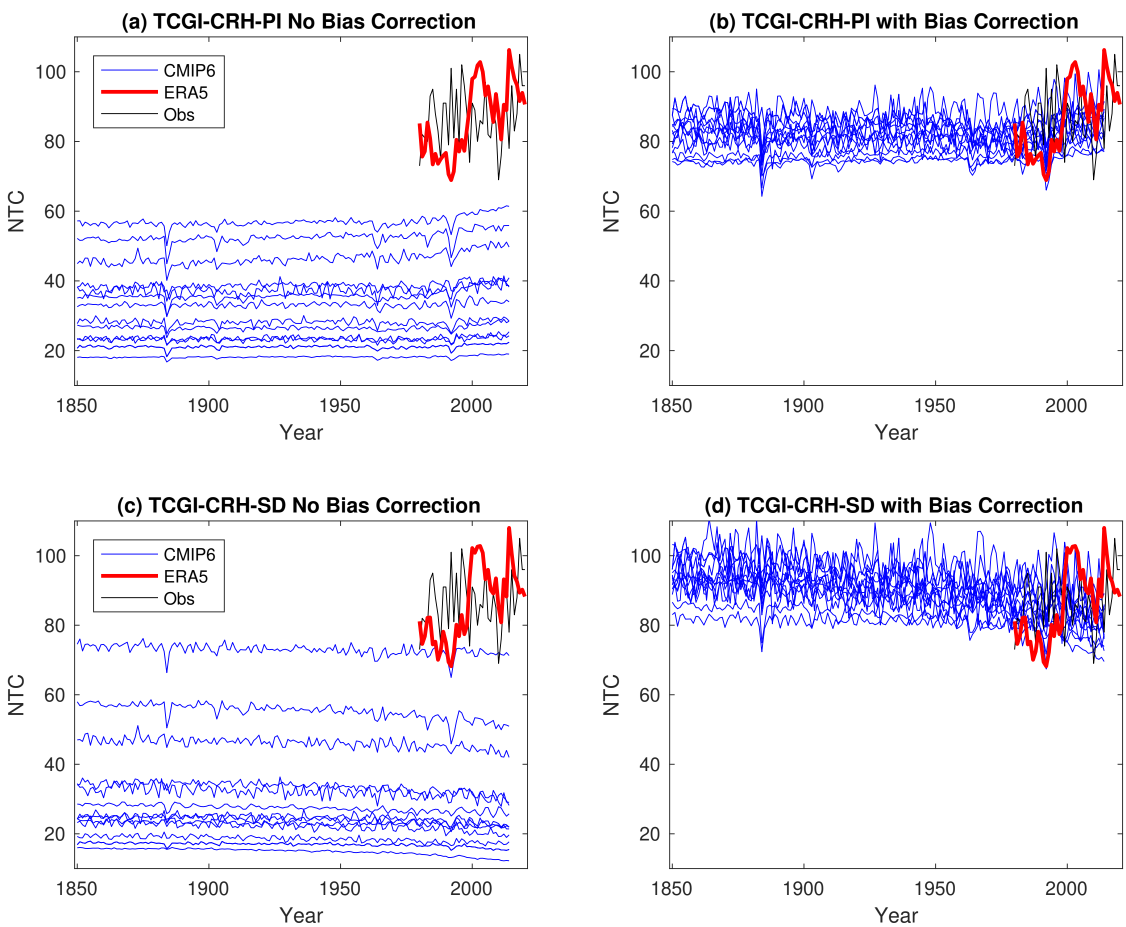

357 FIG. 6. Integrated TCGI time-series (in TC counts) for a subset of CMIP6 models (ensemble mean of each model) using CRH and SD, without bias correction ((a) and (c))) and with bias correction ((b) and (d)). Also shown are the values of the corresponding integrated TCGI for ERA5 and the observed number of TCs. The 13 selected CMIP6 models are underlined in Tables 1 and 2.

The low values in model TCGI has consequences for simulated TCGI variability and change. Since TCGI depends exponentially on environmental fields, additive biases in environmental fields result in multiplicative biases in TCGI. To see this fact, suppose for simplicity that TCGI depends on a single (unitless) environmental field X and that $\mathrm{TCGI}_{\mathrm{obs}} = \exp(X_{\mathrm{obs}})$. Then for a biased model environmental field $X_{\mathrm{model}} = X_{\mathrm{obs}} + \mathrm{bias}$, the corresponding (biased) $\mathrm{TCGI}_{\mathrm{model}}$ is $\exp(\mathrm{bias})\exp(X_{\mathrm{obs}}) = \exp(\mathrm{bias})\mathrm{TCGI}_{\mathrm{obs}}$. Suppose the environmental field is changed by ΔX so that $X'_{\mathrm{model}} = X_{\mathrm{obs}} + \mathrm{bias} + \Delta X$ where ΔX might represent either year-to-year variability or climate change. Since $X'_{\mathrm{model}} - X_{\mathrm{model}} = \Delta X$, the change in the environmental field is recovered by simply subtracting, which cancels the additive bias. On the other hand, $\mathrm{TCGI}'_{\mathrm{model}} - \mathrm{TCGI}_{\mathrm{model}} \approx \Delta X \exp(\mathrm{bias})\mathrm{TCGI}_{\mathrm{obs}}$, for small ΔX, while $\mathrm{TCGI}'_{\mathrm{obs}} - \mathrm{TCGI}_{\mathrm{obs}} \approx \Delta X\ \mathrm{TCGI}_{\mathrm{obs}}$. These relations show that (i) a change in X results in a percent change in TCGI, (ii) those percent changes will also be biased low if $\mathrm{TCGI}_{\mathrm{model}}$ is biased low, and (iii) bias correcting X_{model} and X'_{model} will give the correct change in TCGI due to ΔX.

We bias correct the four environmental fields that appear in the two versions of TCGI. The bias correction consists of subtracting the 1981–2010 model climatology to form an anomaly δ, and then adding the 1981–2010 ERA5 climatology to this δ. The CMIP6 monthly climatology is calculated from the ensemble mean for each model.

The bias-corrected fields are then used to calculate the bias-corrected TCGIs. The integrated bias-corrected TCGI time-series are shown in Figs. 6 (b) and (d). The mean integrated values of the bias-corrected TCGI are much closer to the ERA5 and observed TC values, even though there is still a spread across models in the possible range of values. Note as well the year to year variability, which is clearly too small for all models, improves with the bias correction, even though only the mean values of each field are used in the bias correction.

To determine if one of the four variables in the TCGI versions was primarily responsible for the TCGI bias, we recalculate the TCGI, using one bias-corrected variable at a time and the remaining variables without bias correction. For all 13 CMIP6 models examined, the CRH (or SD) variable is primarily responsible for the TCGI biases. Bias correcting CRH (or SD) alone is sufficient to obtain values of the integrated TCGI close to the ones from ERA5, which does not happen with the other 3 variables. Therefore, the humidity variables (CRH and SD) are responsible for the very low biases of TCGI in the CMIP6 models.

We use the bias-corrected version of the TCGI in the rest of this manuscript for all models and scenarios, using bias-corrected values for the four components of TCGI. However, we do not apply the bias correction to the other genesis indices or other environmental fields or proxies. In most climate model papers which did a similar analysis no bias-correction is applied (e.g., Camargo 2013; Camargo et al. 2014; Wehner et al. 2015; Cavicchia et al. 2023). One exception is the recent manuscript of Wehner and Kossin (2024), which bias-corrected the PI based on ERA5.

d. TC activity

Given the typical low resolution of the CMIP6 models (100 km), it is expected that the climatological features of their TC-like storms will have large biases — typically too few, weak and large storms — similarly to CMIP5 models (Camargo 2013; Camargo and Wing 2016). The biases in TC frequency can be noticed in the historical track density climatology (1981–2010) shown in Fig. 7. While the spatial distributions of the CMIP6 models' track densities somewhat resemble those found in observations and ERA5, there are clear spatial biases in the models. In the North Pacific, most models do not have a clear separation between the eastern and western basins, but rather they are overactive in the Central North Pacific such that they show a continuous band of activity. Most models also do not reproduce the higher TC activity in the northern hemisphere compared with the southern hemisphere. The low TC activity in the North Atlantic is a common bias in climate models (Shaevitz et al. 2014; Roberts et al. 2020a) and there is some improvement in the higher resolution versions of the same models (Roberts et al. 2020a).

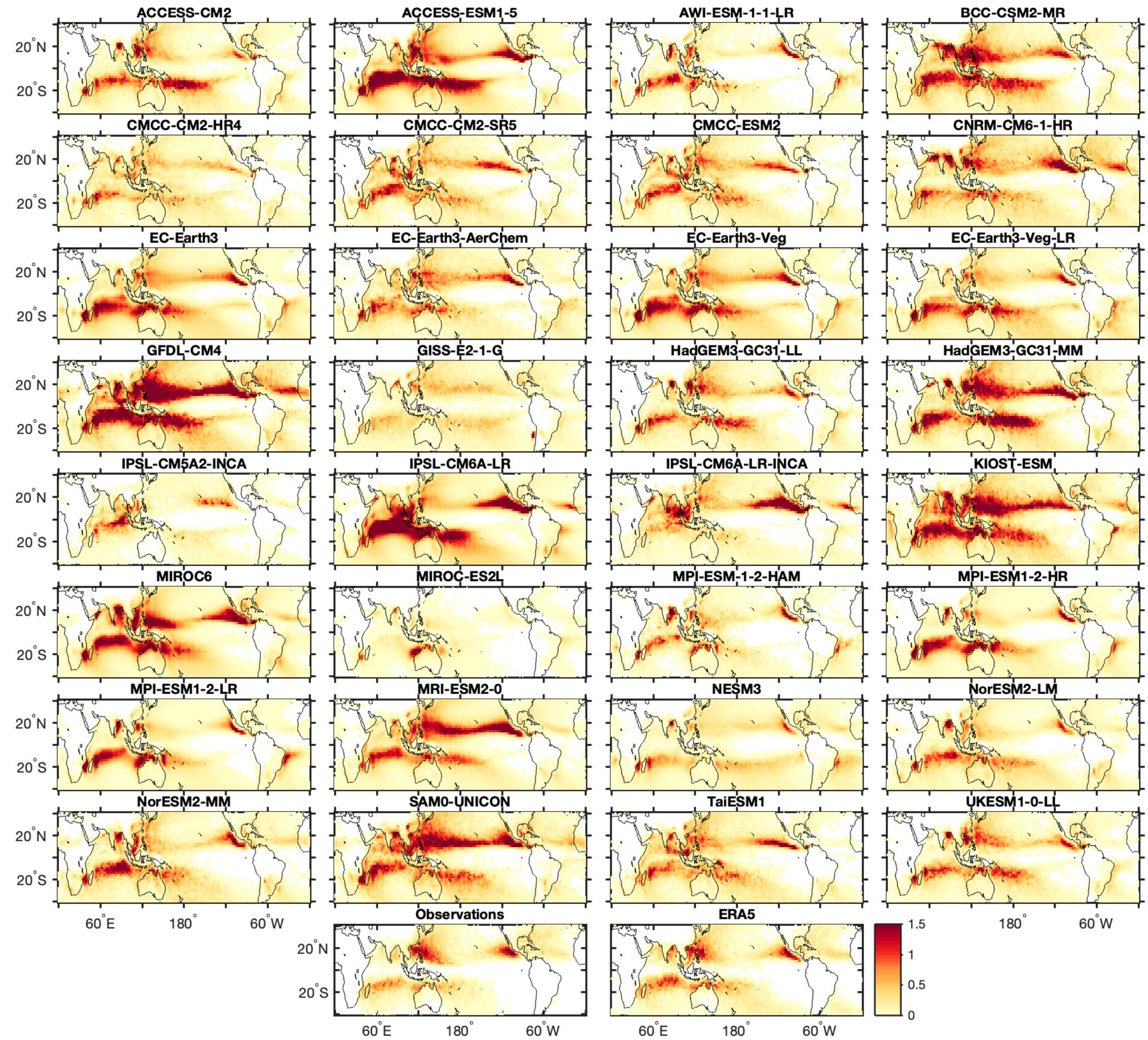

FIG. 7. Track density ensemble mean climatology for 1981–2010 for 32 CMIP6 models, observations and ERA5, shown in units of number of TCs per year.

Typically, as resolution increases, model performance in simulating TC characteristics improves (Shaevitz et al. 2014; Roberts et al. 2020a), though that is not necessarily always the case (Camargo et al. 2020; Moon et al. 2020). In Fig. 8 the relationship between the models' mean NTC and ACE and resolution is shown. While both the TC numbers and their intensities tend to increase as grid spacing becomes smaller, this is not always the case, with models with the same resolution having different values of NTC and ACE, reflecting the importance of other model characteristics, such as physical parametrizations (Vidale et al. 2021; Russotto et al. 2022). There is a stronger correlation between ACE and model resolution than between NTC and resolution, showing the impact of resolution in simulating TC intensity (Murakami et al. 2015; Davis 2018).

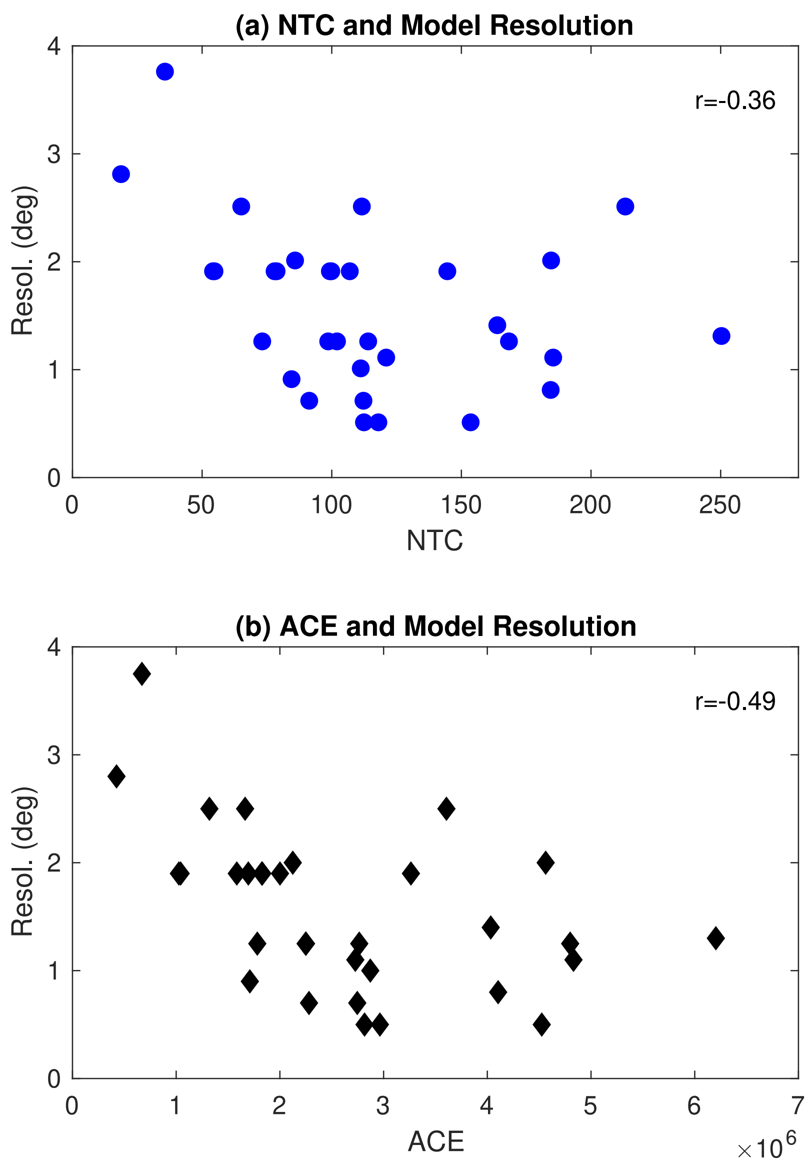

FIG. 8. Scatter plots of the historical climatological mean number of TCs (NTC) per year and climatological mean ACE $(m/s)^2$ per year as a function of model resolution, as listed in Tables 1 and 2, using the largest grid spacing. Values of the Spear correlations are given in the top left of each panel.

e. Environmental fields and TC activity

There is little evidence that climatological environmental conditions can explain differences in climatological TC characteristics across models and reanalyses (Camargo et al. 2020; Dirkes et al. 2023). Here we examine whether there is a relation between climatological model fields and the mean TC climatology in the CMIP6 models, as this has not yet been done. Furthermore, both versions of TCGI are bias-corrected, which was not the case in our CMIP5 analysis, and we want to determine if this leads to different results. In contrast to Camargo et al. (2020) here we consider multiple genesis indices (two versions of TCGI, GPI, GPI-Xi) and the ventilation index in our analysis.

The relationship between NTC and four genesis indices and the ventilation index is shown in Fig. 9 (a)–(d). Similarly to Camargo et al. (2020) and Dirkes et al. (2023) there is no relationship between NTC and the indices. Importantly, this result hold for all the genesis indices considered. While for both TCGI versions, the models' climatological fields have been bias corrected, that was not done for the other indices (GPI, GPI-Xi, VI), and our results are not sensitive to that. GPI and GPI-Xi were normalized, in order to be compatible with TCGI, but that normalization does not affect the correlations.

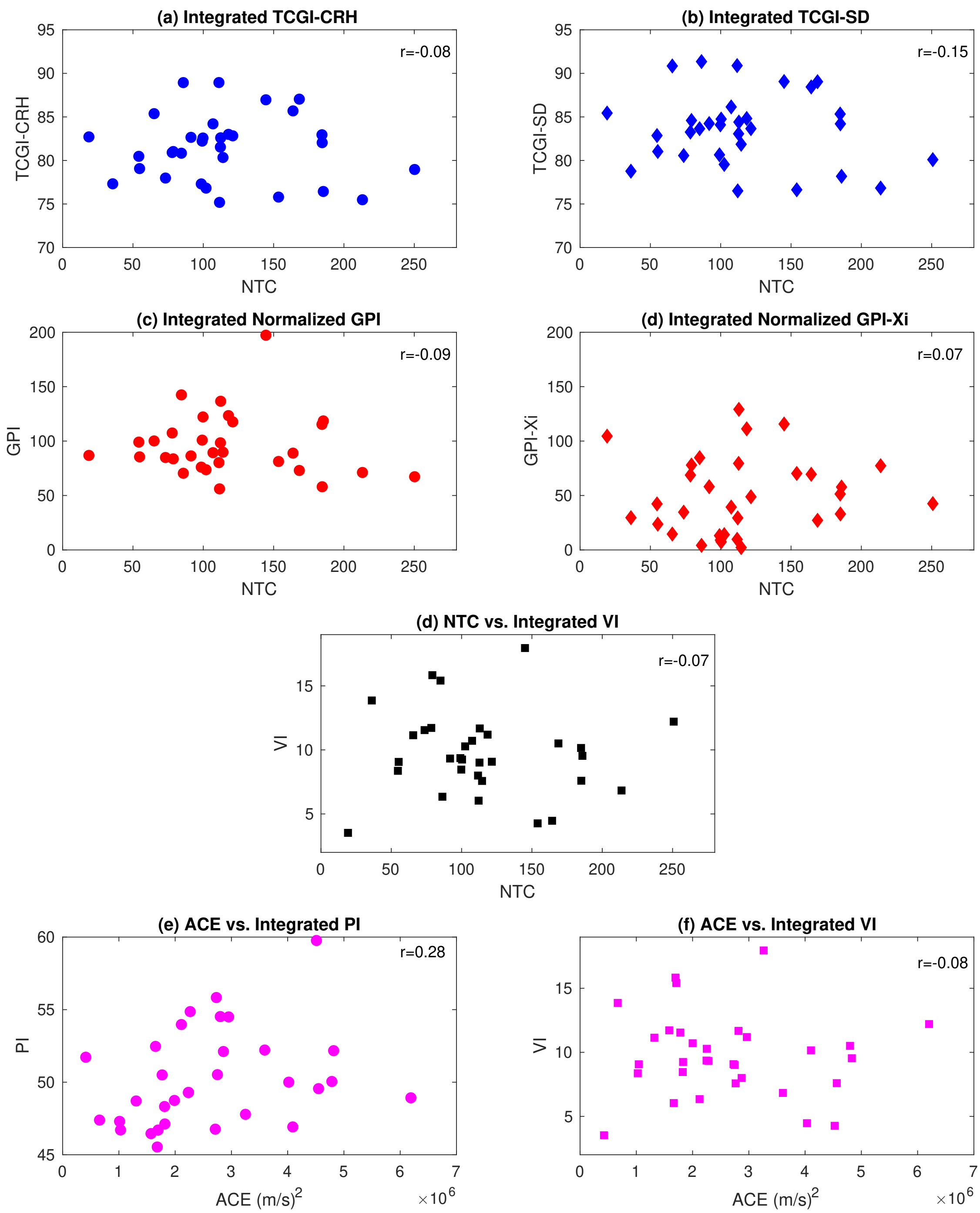

FIG. 9. Scatter plots of the historical climatological mean number of TCs (NTC) and integrated (a) TCGI-CRH, (b) TCGI-SD, normalized integrated (c) GPI, (d) GPI-Xi, and integrated (e) VI. Scatter plots of the historical climatological mean ACE and integrated (f) PI, and (g) VI. The values of the Spear correlations in each case are given in the top left of each panel.

The relationship between ACE and PI, as well as between ACE and the ventilation index, are shown in Figs. 9(e) and (f). The strongest relationship is between PI and ACE, discussed in Ting et al. (2015, 2019); Sobel et al. (2016), but this relationship does not explain the differences in models' TC intensities.

Differences in climatological environmental fields across CMIP6 models do not explain the differences in the models' TC climatology. Other model characteristics, such as physical parameterizations and dynamical core, determine TC climatology in models (e.g. Reed et al. 2015; Russotto et al. 2022)

5. Results - Future Projections

a. Spatial patterns - differences 21C & 20C

We next examine how the environmental fields change between the end of the 21st (2071-2100) projections and the end of the 20th century (1971-2000) historical simulations. Figure 10 shows the differences in the multi-model means for the three future scenarios and five environmental fields. The top panels show the difference between the SSP2-4.5 scenario and historical, while the mid panels and bottom panels represent the SSP3-7.0 and SSP5-8.5 differences, respectively.

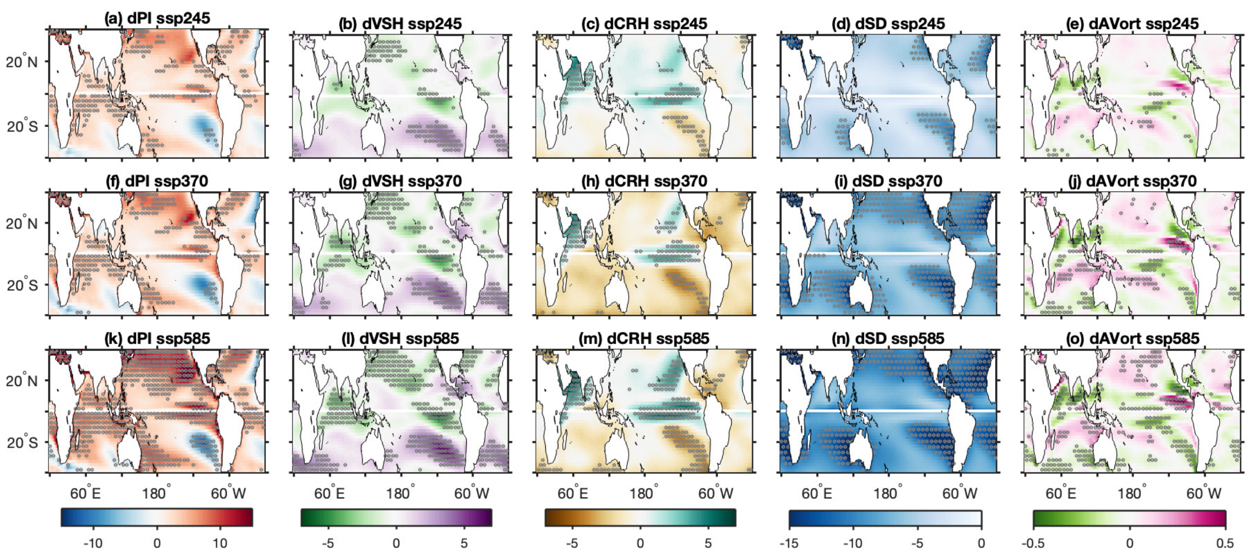

FIG. 10. Difference ("d") between the multi-model mean climatology in the end of the 21C (2071-2100) and the end of 20C (1971-2000) for the 3 future scenarios (SSP2-4.5, SSP3-7.0, SSP5-8.5) for the variables used in TCGI: PI (panels (a),(f), and (k) in m/s), VSH (panels (b), (g) and (l) in m/s), CRH (panels (c), (h) and (m), in %), SD (panels ((d), (i), and (n) in kg/m^2), and absolute vorticity at 850 hPa (AVort, panels (e), (j), and (o) in 10^{-4} 1/s). Stippled regions are statistically significant at the 99% level using a the Kolmogorov-Smirnov significance test.

The potential intensity (Fig. 10 (a), (f) and (k)) increases in most of the tropics, except some regions in the eastern North Atlantic, South Pacific and South Atlantic. As expected, the PI magnitude change is larger the higher the emission scenario, with the largest increases (subtropical North Pacific) and decreases (South Pacific) occurring in the SSP5-8.5 scenario. The number of grid points in which the changes are statistically significant also increases with the emission scenario. In the North Atlantic, North Pacific and South Pacific, the PI increases in large regions in the subtropics, which have been associated with the poleward shift in lifetime maximum intensity (Kossin et al. 2014, 2016; Lin et al. 2023a). Furthermore the patterns in the PI change for the CMIP6 models are very similar to those of CMIP5 (Camargo 2013) and CMIP3 models (Vecchi and Soden 2007a,b).

In the northern hemisphere, there are statistically significant decreases in VSH in many regions (Fig. 10 (b), (g), (l)), in particular in the North Pacific and North Atlantic and in SSP5-8.5. The exception is the Gulf of Mexico and Caribbean region, where the VSH increases. In the southern hemisphere, the magnitude of the VSH increases, but mostly in regions not prone to the occurrence of TCs, such as the South Atlantic, southeast Pacific, and the near South Africa, though hybrid and sub-tropical storms do occur in these regions. Close to the equator in both hemispheres, the magnitude of the VSH decreases, in particular in the tropical equatorial eastern Pacific and in the Indian Ocean. The pattern of the VSH changes in CMIP6 are very similar to those from CMIP5 Camargo (2013); Ting et al. (2019)) and CMIP3 (Vecchi and Soden 2007a,b)

In the tropical Pacific, the CRH increases in both hemispheres (Fig. 10 (c), (h), (m)), as well as in the eastern North Pacific poleward of 20°N. There are also significant increases in the CRH in the North Indian Ocean. Regions with a decrease in the CRH are the Gulf of Mexico and Caribbean, as well as the southeast Pacific, especially for the SSP5-8.5 scenario.

In contrast, the SD decreases globally (Fig. 10 (d), (i), (n)), as was the case for the CMIP5 models (Lee et al. 2020a). Statistically significant decreases in the SD occur in most of the North Atlantic, the subtropical North Pacific and the eastern parts of the southern hemisphere oceans.

The relative vorticity has a bimodal pattern in changes in the eastern tropical Pacific, with an increase close to the tropics and an increase north of that, as well as in the Caribbean. The vorticity also increases in regions of active TC activity in a zonal band near Australia, as well as in the subtropical North Pacific. Regions in which the vorticity decreases coincide with increases in

VSH, such as the southeast Pacific, south of Australia and South Africa and in the North Indian Ocean, but these are not regions in which genesis tends to occur, as it is only necessary for the vorticity to be above certain threshold for genesis to be possible Tippett et al. (2011).

We analyzed the change of the same five environmental fields using the increase per global warming level following Seneviratne and Hauser (2020). The resulting changes are shown in Fig. 11 for 1.5°C, 3°C and 4°C differences from the 19C climatology shown in each row. The number of models used in each composite depends on the warming rate of each model. The patterns are exactly the same as those obtained at the end of the 21C for the three emission scenarios. The changes for 1.5°C are weaker than those in SSP2-4.5 at the end of the 21C, those for 3°C are similar to the latter, and the 4° warming changes are similar to those in SSP5-8.5 at the end of the 21C. The close similarity between Figs. 10 and 11 is remarkable and emphasizes the robustness of changes in these environmental fields. This does not mean the changes need be correct as representations of the response to radiative forcings, however, since some of these responses are likely attributable to the patterns of change in the tropical Pacific, which have been questioned due to their inconsistency with recent historical trends (Sobel et al. 2023).

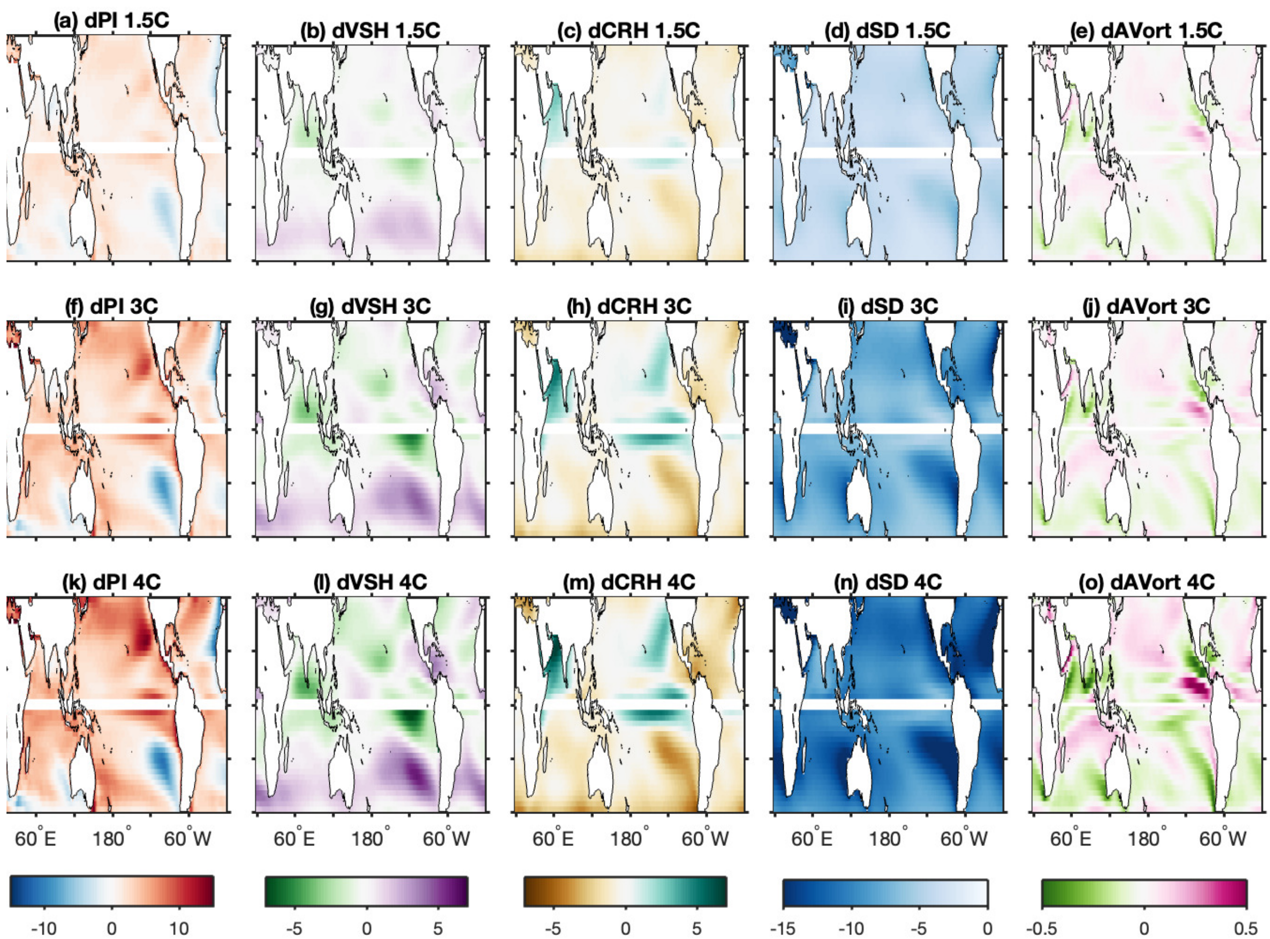

Fig. 11. Difference ("d") between the multi-model mean per global warming level and the 19C climatology (1850–1900) for 1.5°C, 3°C and 4°C for the variables used in TCGI: PI (panels (a),(f), and (k) in m/s), VSH (panels (b), (g) and (l) in m/s), CRH (panels (c), (h) and (m), in %), SD (panels ((d), (i), and (n) in kg/m^2), and absolute vorticity at 850 hPa (AVort, panels (e), (j), and (o) in 10^{-4} 1/s).

Next we analyze changes in the genesis indices by global warming level in Fig. 12.TCGI-CRH and TCGI-SD are shown in Fig. 12 left column and second column from the left). As discussed in Camargo et al. (2014) and Lee et al. (2020b) for the HiRAM and CMIP5 models, TCGI-CRH increases with global warming, while TCGI-SD decreases, and the same behavior is found here for the CMIP6 models. Similar to other environmental fields, the changes in TCGI increase with the amount of warming. The only region in which TCGI-CRH decreases is in the Gulf of Mexico and both coasts of Central America, where the VSH increases with warming. GPI (Fig. 12, second to right column) values increase with global warming for CMIP6 models, as was the case for the CMIP5 (Camargo 2013) and CMIP3 models (Vecchi et al. 2013), indicating a more conducive environment for genesis. GPI-Xi (Emanuel 2010) also increases in the CMIP5 (Emanuel 2013) and CMIP6 simulations (Emanuel 2021). Note that changes in genesis indices are restricted to narrow bands associated with each basin's main development region.

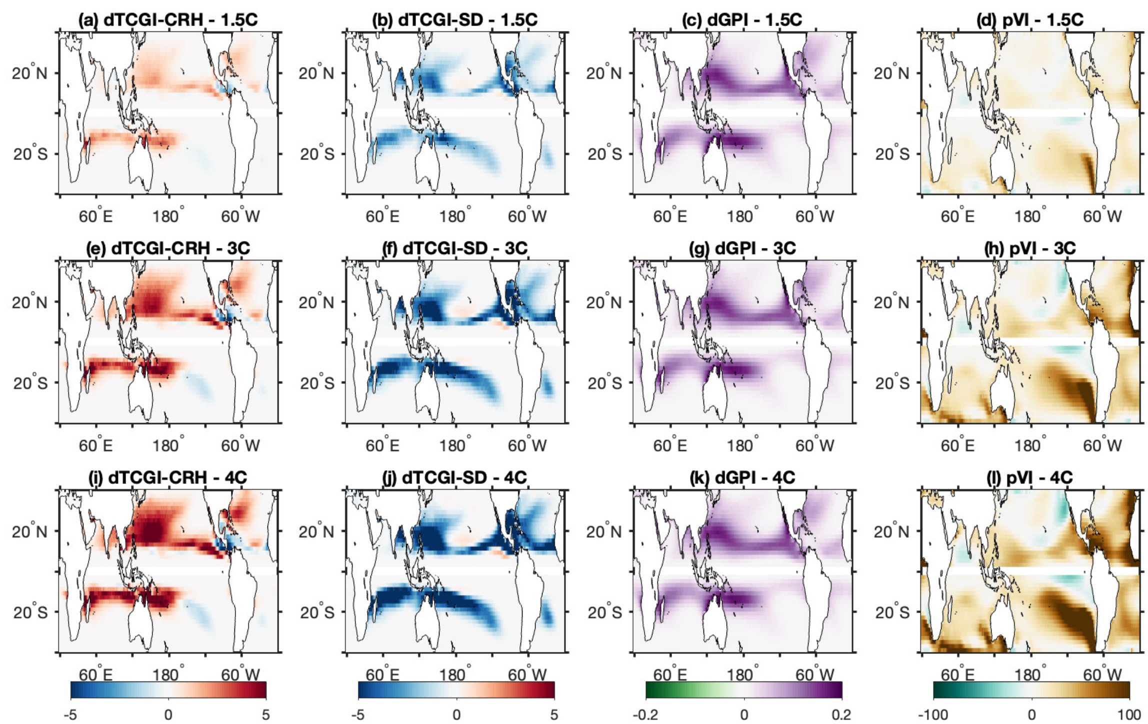

FIG. 12. Difference "d" between the multi-model mean per global warming level and the 19C climatology (1850–1900) for 1.5°C, 3°C and 4°C for TCGI-CRH (panels (a), (e), and (i), NTC per area per year $\times 10^{-3}$), (b) TCGI-SD (panels (b), (f), and (h), NTC per area per year $\times 10^{-3}$), and GPI (panels (i), (j), and (k), unitless). (d) Percentage change per global warming level for the Ventilation Index (pVI).

The final variable that we examine in Fig. 12 (right panels) is the VI (Tang and Emanuel 2010, 2012). The pattern of the percentages changes in the VI by degree warming for the CMIP6 models are very similar to those found previously in Tang and Camargo (2014) for eight CMIP5 models in the RCP5.85 scenario. In most locations the VI increases, with decreases occurring in very few locations, in particular near the equatorial region, near Hawaii, subtropical regions of the eastern North Pacific and the Arabian Sea. Higher values of the VI are characterized by more hostile conditions for TC genesis and intensification. Therefore according to this measure, globally the environment is becoming more hostile for TCs, but the largest changes occur in regions that typically do not have TC formation, as the southeast Pacific, Northeast Atlantic, south of Australia and South Africa. Regions with an increase in the VI are the Gulf of Mexico and Caribbean, where the VSH, a component of VI, increases. These changes extend through the whole Atlantic basin, toward the African coast, until the equatorial region. Note that the changes of the genesis indices in the North Atlantic tend to be very small for GPI and TCGI-CRH.

While in the literature a single genesis index or the ventilation index is regularly used to make TC projections, Fig. 12 indicates that the choice of the index is the main determinant of the future projections of TC activity. Since there is no consensus regarding which index is best, we conclude that choosing a single index to make TC future projections severely underestimates the uncertainty of future TC projections.

b. Potential Intensity Projections and Aerosol Forcing

The global annual mean temperature increase (ΔT) from the 1981–2010 climatology for the historical and the three future scenarios is shown in Fig. 13(a). The thick lines are the MMM of the polynomial fit of the ensemble mean of each model, with the colors indicating the standard deviation across models. A similar calculation was performed showing the increase in the PI (ΔPI) in the northern hemisphere in ASO (Fig. 13(b)) and in the southern hemisphere in JFM (Fig. 13(c). The PI increase is much larger in the northern hemisphere than the southern hemisphere, for all scenarios. For instance, by the end of the 21C the mean tropical PI increase in the northern hemisphere is slightly above 4 m/s for the SSP5-8.5 scenario, while it is around 1.5 m/s in the southern hemisphere. This difference was also present in the CMIP5 models (Sobel et al. 2016).

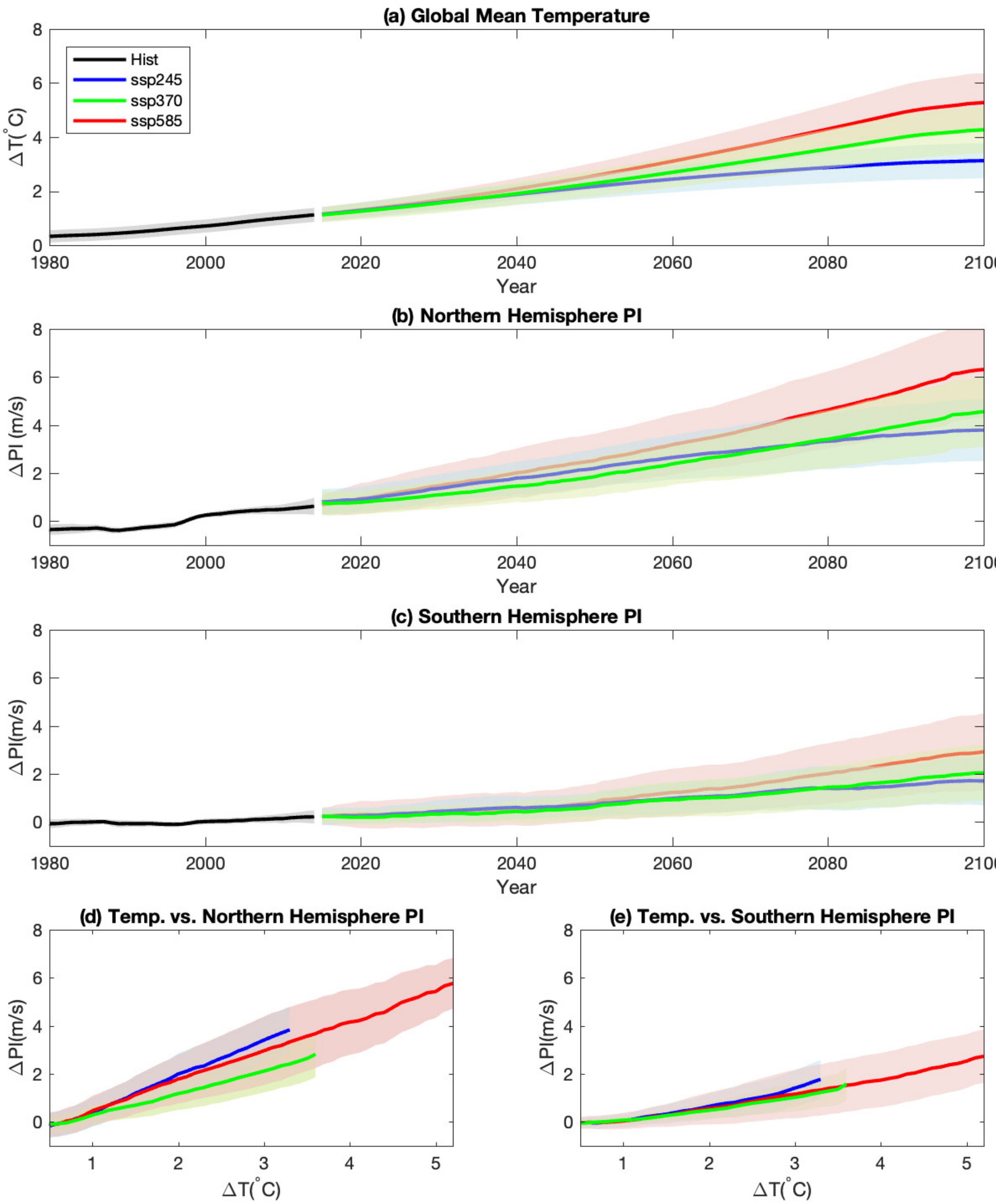

FIG. 13. (a) Global annual mean temperature increase (ΔT in $^{\circ}C$) as compared with the 1981-2010 climatology. (b) Northern hemisphere tropics PI increase (ΔPI in m/s) in ASO. (c) Southern hemisphere tropics potential increase (ΔPI in m/s) in JFM. Lines are the multi-model mean of the polynomial fit of the ensemble mean of each model, colors indicate the standard deviation across models in each scenario. Relationship between ΔT and ΔPI in the (d) northern and (e) southern hemisphere tropics in ASO and JFM respectively. Only ΔT values with at least 15 models are shown.

Another interesting feature, is that while the MMM global mean temperature for the SSP3-7.0 scenario is always above that in the SSP2-4.5 scenario, this is not the case for PI. This is clearer in the northern hemisphere, where the values of PI in SSP3-7.0 are below those in SSP2-4.5 until after 2070, while in the southern hemisphere this does not occur until close to 2080.

Another way to visualize the difference between temperature and PI is to plot the relationship between ΔT and ΔPI for both hemispheres (Fig.13(d),(e)). Only cases in which ΔT values include at least 15 models are plotted. ΔPI increases faster with ΔT in both hemispheres for the SSP2-4.5 scenario than for SSP3-7.0 scenario, in spite of the SSP3-7.0 having higher CO_2 concentrations than SSP2-4.5. This difference is due to the fact that the SSP3-7.0 has a higher aerosol forcing than the SSP2-4.5 scenario. As described in Rao et al. (2017), SSP3-7.0 has a weak pollution control scenario, while SSP2-4.5 scenario has a medium pollution control scenario and SSP5-8.5 has a strong pollution control scenario. Therefore SSP3-7.0 has a stronger aerosol forcing than both other future scenarios considered here. Lund et al. (2019) estimated that the total radiative forcing of aerosols relative to 1750 was around -0.5 W/m^2 for the SSP3-7.0 scenario, compared with -0.2 W/m^2 for the SSP2-4.5 scenario.

As shown in Sobel et al. (2019) and in Ting et al. (2015) using single forcing CMIP5 model simulations, aerosol cooling reduces PI more strongly than greenhouse gas warming increases PI by approximately a factor of two. Given that the aerosol forcing in SSP3-7.0 is relatively stronger than that in SSP2-4.5, we infer that the aerosol cooling in the SSP3-7.0 simulations is compensating for the warming due to the greenhouse gases to yield a PI increase slower than in the case of SSP2-4.5. In the case of the global mean surface temperature, however, aerosol and greenhouse gas forcings are equivalent, and all that matters is the net radiative forcing rather than its partitioning into shortwave and longwave components. As shown in Sobel et al. (2019) the greater effect of aerosol forcing is due to the fact that the shortwave forcing has a greater direct, temperature-independent component at the surface than longwave forcing for the same SST change, the latter of which was also shown using a single column model by Emanuel et al. (2013). It is interesting that this effect is clearly noticeable in simple time-series of ΔPI when comparing these two future scenarios.

c. Potential Intensity Projections and Model Sensitivity

It is well known that the amount of warming for the same amount of greenhouse forcing varies across models, including the CMIP6 models. In particular, Hausfather et al. (2022) argued that when performing MMM averages, one should exclude models that overestimate the future warming. Based on evidence from paleoclimate, observations and modeling, they concluded that the equilibrium climate sensitivity (ECS) is very likely to be in the range 2.6 – 3.9°C and that models with high climate sensitivity (ECS of at least 5°C) are considered "too hot". Here we examine how PI projections vary depending on whether we consider the MMM of all CMIP6 models, or only the models that are have the "right" model sensitivity, i.e., if we exclude the models that are "too hot". Following Hausfather et al. (2022)'s classification of the CMIP6 models, we calculated the mean increase in tropical PI in each hemisphere for ASO (northern hemisphere) and JFM (southern hemisphere) at the end of the 21C (2091 – 2100) compared with the 1981 – 2010 climatology (Fig. 14). In the northern hemisphere, the ΔPI is statistically significantly different at the end of the 21C for the SSP3-7.0 and SSP5-8.5 scenarios, between the two multi-model averages, with the median of the multi-model of the "right models" slightly smaller than that of all models, and the difference increasing with the warming scenario, i.e., lowest for SSP2-4.5, highest for SSP5-8.5. The same occurs in the southern hemisphere, but as the ΔPI is smaller in that hemisphere, the differences between the multi-model mean are smaller and are not statistically significant. Note that even in the case with the largest difference between the two multi-model means, i.e., northern hemisphere for SSP5-8.5, these differences are still small. The effect of considering the "too hot" models is not large for the seasonal mean PI.

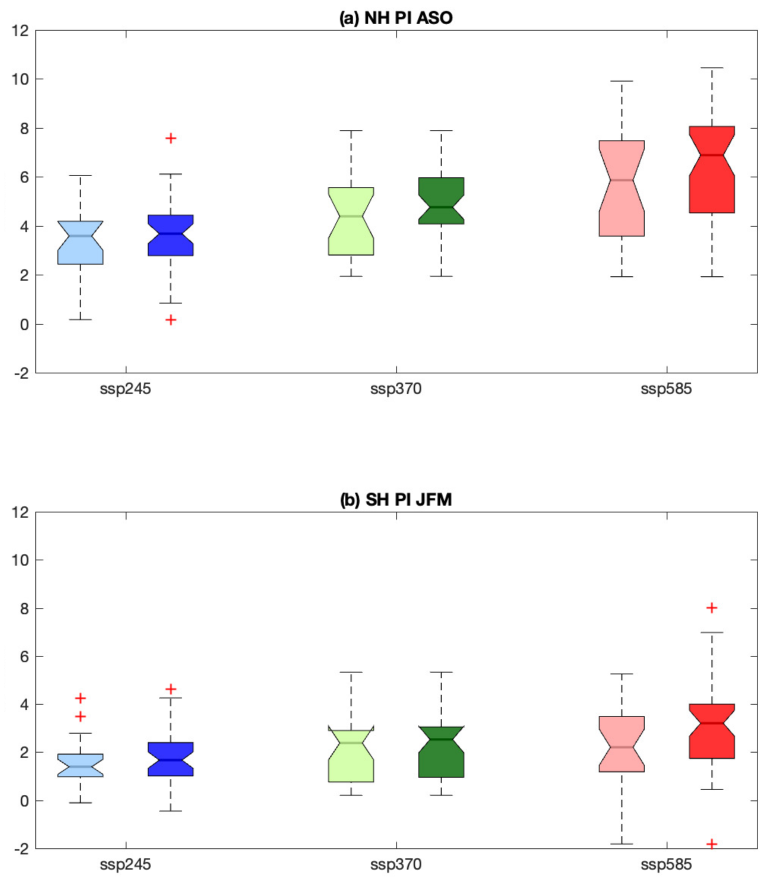

FIG. 14. PI increase (in m/s) at the end of the 21C (2091 – 2100) compared with the 1981 – 2010 climatology for all models (dark colored boxplots on the right) and models with the "right" climate sensitivity (lighter colored boxplots on the left) in the northern hemisphere for ASO (top panel) and southern hemisphere for JFM (bottom panel), for 3 future scenarios SSP2-4.5 (blue), SSP3-7.0 (green), SSP5-8.5 (red). Not all models considered here have ECS values available.

Figure 15 shows the scatter plots of the increase in PI (dPI) at the end of the 21C (2091 – 2100) from the end of the 20C (1981 – 2010) and the models' ECS in the northern (a) and southern (b) hemisphere, using the ECS values from Hausfather et al. (2022). Only models with ECS listed in Hausfather et al. (2022) were included. The correlation between dPI and ECS varies between 0.38 and 0.50 depending on the future scenario and hemisphere considered, and it is statistically significant in all cases. While there is a clear relationship between these two quantities for all cases, in both hemisphere the lowest correlation occurs for SSP3-7.0, the scenario with the highest aerosols concentration, which should not be surprising, as ECS only considers changes in CO_2. However, it is important to note that there is large spread in dPI values for models with the same ECS and scenario. In the northern hemisphere the highest dPI values per ECS value are typically from SSP5-8.5 and the lowest from SSP2-4.5, with SSP3-7.0 in between them. This separation does not work as well in the southern hemisphere, with the dPI values from the 3 future scenarios more mixed.

d. NTC and ACE projections

We now examine how the characteristics of the models' TCs changed between the end of the 20C and the 21C. There are only 20 models which have the TCs tracked for both historical and SSP5-8.5, marked with a star in Tables 1 and 2.

The percentage change in the median global NTC per year between the two 30-year periods for each model is shown in Fig. 16(a). In most models there is a reduction in the global annual frequency of TCs, similar to past studies e.g., Camargo (2013); Roberts et al. (2020b). Again this is in contrast with the increase in most genesis indices shown in Fig. 12, except TCGI-SD, as discussed in Camargo et al. (2014); Lee et al. (2020a, 2023).

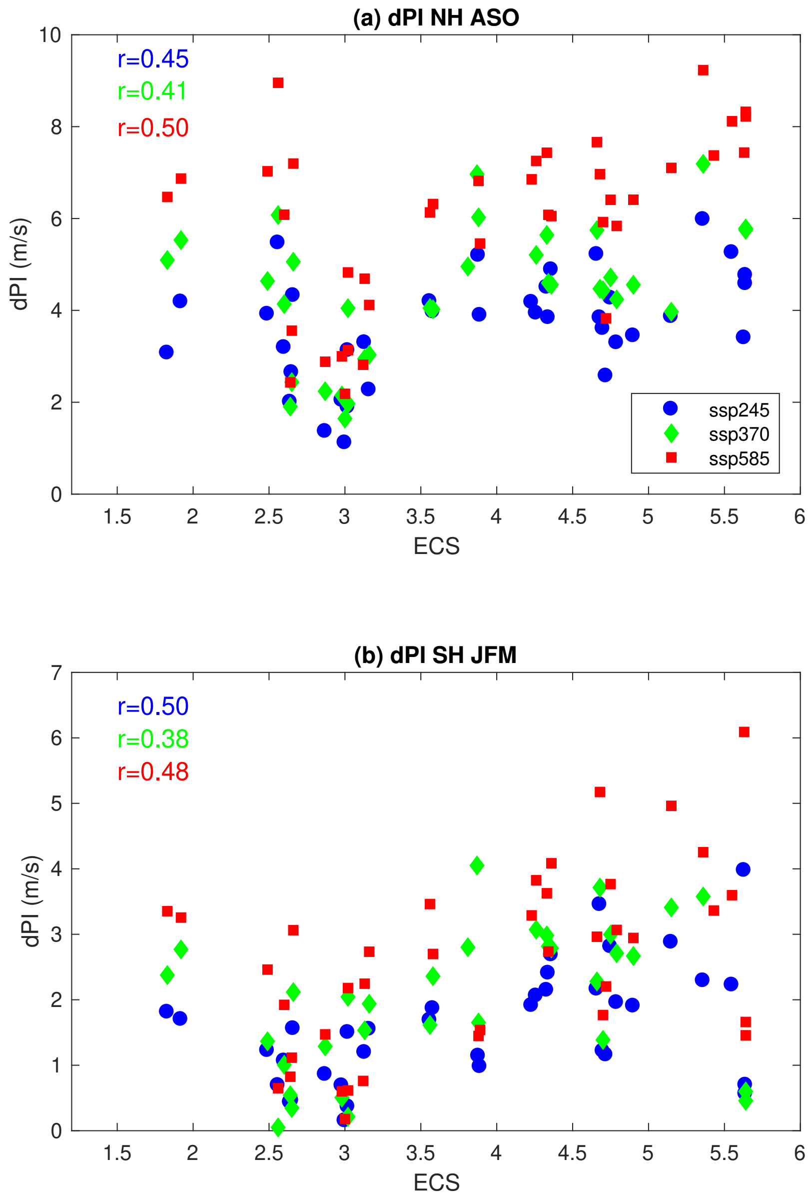

FIG. 15. Scatter plots of increase in PI in m/s at the end of 21C (2091-2100) from the end of the 20C climatology (1981-2010) versus ECS values from Hausfather et al. (2022) for the (a) northern hemisphere in ASO and (b) southern hemisphere in JFM,for 3 future scenarios SSP2-4.5 (blue), SSP3-7.0 (green), SSP5-8.5 (red). The correlation values for each scenario and hemisphere are given in each panel. Not all models considered here have ECS values available.

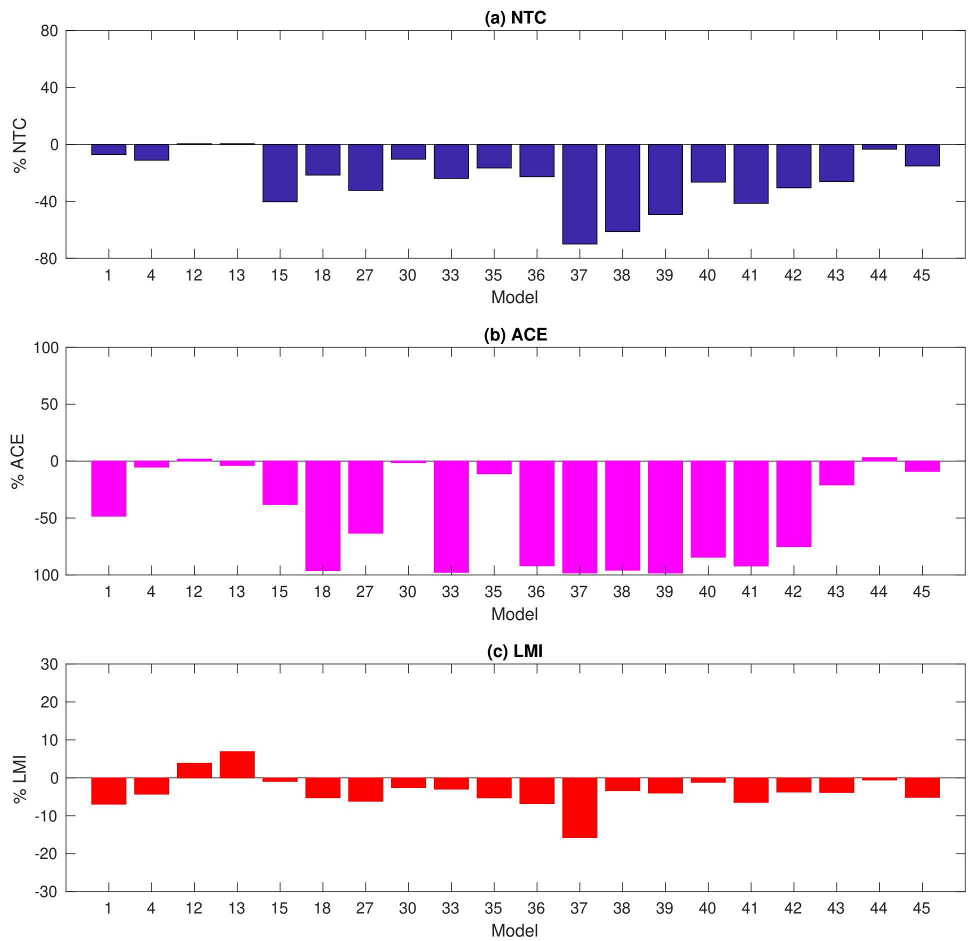

644 FIG. 16. Percentage change between the models ensemble mean in 2071-2100 compared with 1971-2000 for
645 (a) Median global NTC, (b) Median global ACE, (c) 75 percentile of Lifetime Maximum Intensity (LMI).

The percentage change in the median ACE per year between future and historical scenarios is shown in Fig. 16(b). Similar to NTC, there is a large decrease in ACE across most models. Given that ACE is an integrated measure of frequency (NTC), duration and intensity, we further examined the change in the storms lifetime maximum intensity (LMI). The percentage change in the 75th percentile values of storms LMI is shown in Fig. 16(c). The LMI percentage changes are minimal between the two scenarios. Therefore, the changes in ACE are dominated by changes in the TC frequency, given that the changes in TC duration are not noticeable (not shown).

6. Conclusions

In this manuscript, we examined the characteristics of environmental fields associated with TCs in CMIP6 historical and future simulations, as well as the TC-like storms tracked in these models. We found that TC-associated environmental fields in the CMIP6 models have large biases in their historical climatological patterns, magnitude, and interannual variability compared with ERA5. These biases are present in thermodynamic and dynamic variables. There are clear systematic biases across models from the same modeling centers, as the patterns of the biases are extremely similar. The largest differences among environmental variables climatology across reanalyses are in the humidity fields. Similarly, there is a large spread across models in the climatological values of environmental fields associated with humidity, such as PI and CRH. Furthermore, the variance of all environmental variables examined is much smaller than in reanalysis.

The biases in the individual environmental variables lead to biases in TC proxies such as genesis indices. By bias-correcting the individual components of these indices, before computing them, one can obtain values much closer values to the ERA5 ones. Because of the nonlinearity of the indices' dependences on the individual variables, correcting mean biases in the individual variables improves the biases not just in the mean indices, but in their variability as well. Column humidity is the variable primarily responsible for the bias in the indices, and thus the one whose correction has the greatest impact.

Similarly to CMIP5 and reanalyses products, there is no clear relationship between the mean TC activity (NTC and ACE) and the climatological values of the environmental fields and proxies across CMIP6 models. Furthermore, models with the same horizontal resolution have a large range of NTC and ACE values, even if increased the model resolution leads in general to higher NTC and ACE values in CMIP6 models.

The patterns of the environmental fields in the CMIP6 model projections are very similar to those in CMIP5. These patterns are robust and similar across projection scenarios and GWL. Models with greater climate sensitivity have larger increases in PI, but the differences are only significant for high emissions scenarios and at the end of 21C. Furthermore, the compensation between aerosol and GHG forcings in the PI increase is important, such that the scenarios with high aerosol loading exhibit slower increases in PI.

Projections based on genesis indices are strongly dependent on the formulation of the genesis index used, and projections based on a single genesis index should be taken with extreme caution, as there is no way to determine which genesis index formulation is the "correct" one. In particular, while some formulations of the genesis indices project an increase in TC activity, others project a decrease, in agreement with what is obtained from the diagnostics of TC activity in CMIP6 models (NTC and ACE). Recently, Chavas et al. (2024) developed a new genesis index more heavily based in theory than previous indices. While there is no complete theory for genesis our recommendation is to improve genesis indices using robust theoretical principles. Furthermore, the addition of seeds survival rate into genesis indices, as done in Hsieh et al. (2020) could potentially lead to more robust projections from genesis indices, though there are still conflicting perspectives about this issue (e.g. Emanuel (2022)).

The climatology of TC-like storms in the CMIP6 has significantly improved compared with CMIP5, probably associated with the increase in horizontal resolution across the multi-model ensemble. Other model changes from CMIP5 to CMIP6, such as convective parametrization, are model dependent and could affect TC activity in ways that are not coherent across models. In spite of the increased model resolution, TC activity still shows substantial biases, as the model resolution is still not high enough to resolve TCs. However, models with similar resolution can have a large range of skill in reproducing TC climatology. Similar to previous generations, there is a decline in NTC in the future for most models at the end of the 21C under a high emission scenario.

Systematic biases in the CMIP6 models, such as the trend in the spatial pattern of tropical Pacific SST, need to be addressed in order to obtain a better estimate of the uncertainty range of TC projections, independently of the methodology used.

Acknowledgments. S.J.C, M.K.T, A.H.S, C.-Y.L. and B.F. acknowledge support from Aon/Impact Forecasting for this work. S.J.C. and C.-Y.L also acknowledge support of NSF (AGS 20-43142). We acknowledge the World Climate Research Programme, which, through its Working Group on Coupled Modelling, coordinated and promoted CMIP6. We thank the climate modeling groups for producing and making available their model output, the Earth System Grid Federation (ESGF) for archiving the data and providing access, and the multiple funding agencies who support CMIP6 and ESGF.

Data availability statement. The publicly available CMIP6 multi-model ensemble dataset was used in this paper. CMIP6 ensemble model outputs can be downloaded from the different Earth System Grid Federation (ESGF) nodes. The NOAA's International Best Track Archive for Climate Stewardship (IBTrACS) dataset version 4 was used for tropical cyclones observations (`http://doi.org/0.25921/82ty-9e16`;Knapp et al. (2010, 2018)). Reanalysis data from ERA5 (Hersbach et al. 2020, 2023a,b) were provided by the Copernicus Climate Change Service Climate Data Store (CDS) and are available at `https://cds.climate.copernicus.eu`.

References

Andrews, T., and Coauthors, 2019: Forcings, Feedbacks, and Climate Sensitivity in HadGEM3-GC3.1 and UKESM1. *J. Adv. Model. Earth Sys.*, **11 (12)**, 4377–4394, https://doi.org/10.1029/2019MS001866.

Arias, P. A., and Coauthors, 2021: Technical Summary in *Climate Change 2021: The Physical Science Basis. Contribution of Working Group I to the Sixth Assessment Report of the Intergovernmental Panel on Climate Change*. Cambridge University Press, Cambridge, United Kingdom and New York, NY, USA, 33 - 144 pp., https://doi.org/10.1017/9781009157896.002.

Bao, Y., Z. Song, and F. Qiao, 2020: FIO-ESM Version 2.0: Model Description and Evaluation. *J. Geophys. Res.*, **125 (6)**, e2019JC016 036, https://doi.org/10.1029/2019JC016036.

Baudouin, J.-P., L.-P. Caron, and M. Boudreault, 2019: Impact of reanalysis boundary conditions on downscaled Atlantic hurricane activity. *Clim. Dyn.*, **52 (5)**, 3709–3727, https://doi.org/10.1007/s00382-018-4352-7.

Bell, G. D., and Coauthors, 2000: Climate Assessment for 1999. *Bull. Amer. Meteor. Soc.*, **81 (6)**, S1–S50, https://doi.org/10.1175/1520-0477(2000)81[s1:CAF]2.0.CO;2.

Bell, S. S., S. S. Chand, S. J. Camargo, K. J. Tory, C. Turville, and H. Ye, 2019: Western North Pacific Tropical Cyclone Tracks in CMIP5 Models: Statistical Assessment Using a Model-Independent Detection and Tracking Scheme. *J. Climate*, **32 (21)**, 7191–7208, https://doi.org/10.1175/JCLI-D-18-0785.1.

Bi, D., and Coauthors, 2020: Configuration and spin-up of ACCESS-CM2, the new generation Australian Community Climate and Earth System Simulator Coupled Model. *J. South. Hemisphere Earth Sys. Sci.*, **70 (1)**, 225–251, https://doi.org/10.1071/ES19040.

Bister, M., and K. A. Emanuel, 2002: Low frequency variability of tropical cyclone potential intensity 1. Interannual to interdecadal variability. *J. Geophys. Res.*, **107 (D24)**, 26–15, https://doi.org/10.1029/2001JD000776.

Bloemendaal, N., I. D. Haigh, H. de Moel, S. Muis, R. J. Haarsma, and J. C. J. H. Aerts, 2020: Generation of a global synthetic tropical cyclone hazard dataset using STORM. *Sci. Data*, **7 (1)**, 40, https://doi.org/10.1038/s41597-020-0381-2.

Boucher, O., and Coauthors, 2020: Presentation and Evaluation of the IPSL-CM6A-LR Climate Model. *J. Adv. Model. Earth Sys.*, **12 (7)**, e2019MS002 010, https://doi.org/10.1029/2019MS002010.

Bretherton, C. S., M. E. Peters, and L. E. Back, 2004: Relationships between Water Vapor Path and Precipitation over the Tropical Oceans. *J. Climate*, **17 (7)**, 1517–1528, https://doi.org/10.1175/1520-0442(2004)017⟨1517:RBWVPA⟩2.0.CO;2.

Camargo, S. J., 2013: Global and Regional Aspects of Tropical Cyclone Activity in the CMIP5 Models. *J. Climate*, **26 (24)**, 9880–9902, https://doi.org/10.1175/JCLI-D-12-00549.1.

Camargo, S. J., A. G. Barnston, and S. E. Zebiak, 2005: A statistical assessment of tropical cyclone activity in atmospheric general circulation models. *Tellus A*, **57 (4)**, 589–604, https://doi.org/10.3402/tellusa.v57i4.14705.

Camargo, S. J., K. A. Emanuel, and A. H. Sobel, 2007: Use of a Genesis Potential Index to Diagnose ENSO Effects on Tropical Cyclone Genesis. *J. Climate*, **20 (19)**, 4819–4834, https://doi.org/10.1175/JCLI4282.1.

Camargo, S. J., and A. H. Sobel, 2005: Western North Pacific Tropical Cyclone Intensity and ENSO. *J. Climate*, **18 (15)**, 2996–3006, https://doi.org/10.1175/JCLI3457.1.

Camargo, S. J., M. K. Tippett, A. H. Sobel, G. A. Vecchi, and M. Zhao, 2014: Testing the Performance of Tropical Cyclone Genesis Indices in Future Climates Using the HiRAM Model. *J. Climate*, **27 (24)**, 9171–9196, https://doi.org/10.1175/JCLI-D-13-00505.1.

Camargo, S. J., and A. A. Wing, 2016: Tropical cyclones in climate models: Tropical cyclones in climate models. *WIREs Clim. Change*, **7 (2)**, 211–237, https://doi.org/10.1002/wcc.373.

Camargo, S. J., and Coauthors, 2020: Characteristics of Model Tropical Cyclone Climatology and the Large-Scale Environment. *J. Climate*, **33 (11)**, 4463–4487, https://doi.org/10.1175/JCLI-D-19-0500.1.

Camargo, S. J., and Coauthors, 2023: An update on the influence of natural climate variability and anthropogenic climate change on tropical cyclones. *Trop. Cyclone Res. Rev.*, **12 (3)**, 216–239, https://doi.org/10.1016/j.tcrr.2023.10.001.

Cao, J., and Coauthors, 2018: The NUIST Earth System Model (NESM) version 3: description and preliminary evaluation. *Geosci. Model. Dev.*, **11 (7)**, 2975–2993, https://doi.org/10.5194/gmd-11-2975-2018.

Cavicchia, L., E. Scoccimarro, G. Ascenso, A. Castelletti, M. Giuliani, and S. Gualdi, 2023: Tropical Cyclone Genesis Potential Indices in a New High-Resolution Climate Models Ensemble: Limitations and Way Forward. *Geophys. Res. Lett.*, **50 (11)**, e2023GL103 001, https://doi.org/10.1029/2023GL103001.

Chand, S. S., K. J. Tory, H. Ye, and K. J. E. Walsh, 2017: Projected increase in El Niño-driven tropical cyclone frequency in the Pacific. *Nature Clim. Change*, **7 (2)**, 123–127, https://doi.org/10.1038/nclimate3181.

Chavas, D. R., S. J. Camargo, and M. K. Tippett, 2024: Tropical cyclone genesis potential using a ventilated potential intensity. *J. Climate*, https://doi.org/10.1175/JCLI-D-24-0186.1, early online.

Danabasoglu, G., and Coauthors, 2020: The Community Earth System Model Version 2 (CESM2). *J. Adv. Model. Earth Sys.*, **12 (2)**, e2019MS001 916, https://doi.org/10.1029/2019MS001916.

Davis, C. A., 2018: Resolving Tropical Cyclone Intensity in Models. *Geophys. Res. Lett.*, **45 (4)**, 2082–2087, https://doi.org/10.1002/2017GL076966.

Dee, D. P., and Coauthors, 2011: The ERA-Interim reanalysis: Configuration and performance of the data assimilation system. *Quart. J. Roy. Meteor. Soc.*, **137**, 553–597, https://doi.org/10.1002/qj.828.

Dirkes, C. A., A. A. Wing, S. J. Camargo, and D. Kim, 2023: Process-Oriented Diagnosis of Tropical Cyclones in Reanalyses Using a Moist Static Energy Variance Budget. *J. Climate*, **36 (16)**, 5293–5317, https://doi.org/10.1175/JCLI-D-22-0384.1.

Döscher, R., and Coauthors, 2022: The EC-Earth3 Earth system model for the Coupled Model Intercomparison Project 6. *Geoscientific Model Development*, **15 (7)**, 2973–3020, https://doi.org/10.5194/gmd-15-2973-2022, URL https://gmd.copernicus.org/articles/15/2973/2022/, publisher: Copernicus GmbH.

Dunne, J. P., and Coauthors, 2020: The GFDL Earth System Model Version 4.1 (GFDL-ESM 4.1): Overall Coupled Model Description and Simulation Characteristics. *J. Adv. Model. Earth Sys.*, **12 (11)**, e2019MS002 015, https://doi.org/10.1029/2019MS002015.

Emanuel, K., 1988: The maximum intensity of hurricanes. *J. Atmos. Sci.*, **45 (7)**, 1143–1155, https://doi.org/10.1175/1520-0469(1988)045⟨1143:TMIOH⟩2.0.CO;2.

Emanuel, K., 2000: A Statistical Analysis of Tropical Cyclone Intensity. *Mon. Wea. Rev.*, **128**, 1139–1152.

Emanuel, K., 2010: Tropical cyclone activity downscaled from NOAA-CIRES Reanalysis, 1908–1958. *J. Adv. Model. Earth Sys.*, **2**, 1, https://doi.org/10.3894/JAMES.2010.2.1.

Emanuel, K., 2021: Response of Global Tropical Cyclone Activity to Increasing CO2: Results from Downscaling CMIP6 Models. *J. Climate*, **34 (1)**, 57–70, https://doi.org/10.1175/JCLI-D-20-0367.1.

Emanuel, K., 2022: Tropical Cyclone Seeds, Transition Probabilities, and Genesis. *J. Climate*, **35**, 3557–3566, https://doi.org/10.1175/JCLI-D-21-0922.1.

Emanuel, K., S. Ravela, E. Vivant, and C. Risi, 2006: A Statistical Deterministic Approach to Hurricane Risk Assessment. *Bull. Amer. Meteor. Soc.*, **87 (3)**, 299–314, https://doi.org/10.1175/BAMS-87-3-299.

Emanuel, K., S. Solomon, D. Folini, S. Davis, and C. Cagnazzo, 2013: Influence of Tropical Tropopause Layer Cooling on Atlantic Hurricane Activity. *J. Climate*, **26 (7)**, 2288–2301, https://doi.org/10.1175/JCLI-D-12-00242.1.

Emanuel, K. A., 1987: The dependence of hurricane intensity on climate. *Nature*, **326 (6112)**, 483–485, https://doi.org/10.1038/326483a0.

Emanuel, K. A., 2013: Downscaling CMIP5 climate models shows increased tropical cyclone activity over the 21st century. *Proc. Natl. Acad. Sci. USA*, **110 (30)**, 12 219–12 224, https://doi.org/10.1073/pnas.1301293110.

Emanuel, K. A., and D. S. Nolan, 2004: Tropical cyclone activity and global climate. *Proc. of 26th Conference on Hurricanes and Tropical Meteorology*, American Meteorological Society, Miami, FL, 240–241.

Eyring, V., S. Bony, G. A. Meehl, C. A. Senior, B. Stevens, R. J. Stouffer, and K. E. Taylor, 2016: Overview of the Coupled Model Intercomparison Project Phase 6 (CMIP6) experimental design and organization. *Geosci. Model. Dev.*, **9 (5)**, 1937–1958, https://doi.org/10.5194/gmd-9-1937-2016.

Feng, J., J. Cao, B. Wang, and K. Zhao, 2024: Understanding the Inter-Model Spread of PDO's Impact on Tropical Cyclone Frequency over the Western North Pacific in CMIP6 Models. *Atmosphere*, **15 (3)**, 276, https://doi.org/10.3390/atmos15030276.

Fu, D., P. Chang, C. M. Patricola, and R. Saravanan, 2019: High-Resolution Tropical Channel Model Simulations of Tropical Cyclone Climatology and Intraseasonal-to-Interannual Variability. *J. Climate*, **32 (22)**, 7871–7895, https://doi.org/10.1175/JCLI-D-19-0130.1.

Golaz, J.-C., and Coauthors, 2019: The DOE E3SM Coupled Model Version 1: Overview and Evaluation at Standard Resolution. *J. Adv. Model. Earth Sys.*, **11 (7)**, 2089–2129, https://doi.org/10.1029/2018MS001603.

Gutjahr, O., D. Putrasahan, K. Lohmann, J. H. Jungclaus, J.-S. von Storch, N. Brüggemann, H. Haak, and A. Stössel, 2019: Max Planck Institute Earth System Model (MPI-ESM1.2) for the High-Resolution Model Intercomparison Project (HighResMIP). *Geosci. Model. Dev.*, **12 (7)**, 3241–3281, https://doi.org/10.5194/gmd-12-3241-2019.

Haarsma, R. J., and Coauthors, 2016: High Resolution Model Intercomparison Project (HighResMIP v1.0) for CMIP6. *Geosci. Model Dev.*, **9 (11)**, 4185–4208, https://doi.org/10.5194/gmd-9-4185-2016.

Hajima, T., and Coauthors, 2020: Development of the MIROC-ES2L Earth system model and the evaluation of biogeochemical processes and feedbacks. *Geosci. Model. Dev.*, **13 (5)**, 2197–2244, https://doi.org/10.5194/gmd-13-2197-2020.

Hall, T. M., and S. Jewson, 2007: Statistical modelling of North Atlantic tropical cyclone tracks. *Tellus A*, **59 (4)**, 486–498, https://doi.org/10.1111/j.1600-0870.2007.00240.x.

Hausfather, Z., K. Marvel, G. A. Schmidt, J. W. Nielsen-Gammon, and M. Zelinka, 2022: Climate simulations: recognize the ‘hot model’ problem. *Nature*, **605 (7908)**, 26–29, https://doi.org/10.1038/d41586-022-01192-2.

He, B., and Coauthors, 2019: CAS FGOALS-f3-L Model Datasets for CMIP6 Historical Atmospheric Model Intercomparison Project Simulation. *Adv. Atmos. Sci.*, **36 (8)**, 771–778, https://doi.org/10.1007/s00376-019-9027-8.

Held, I. M., and Coauthors, 2019: Structure and Performance of GFDL’s CM4.0 Climate Model. *J. Adv. Model. Earth Sys.*, **11 (11)**, 3691–3727, https://doi.org/10.1029/2019MS001829.

Hersbach, H., and Coauthors, 2020: The ERA5 global reanalysis. *Q.J.R. Meteorol. Soc.*, **146 (730)**, 1999–2049, https://doi.org/10.1002/qj.3803.

Hersbach, H., and Coauthors, 2023a: ERA5 monthly averaged data on pressure levels from 1940 to present. Copernicus Climate Change Service (C3S) Climate Data Store (CDS), https://doi.org/10.24381/cds.6860a573.

Hersbach, H., and Coauthors, 2023b: ERA5 monthly averaged data on single levels from 1940 to present. Copernicus Climate Change Service (C3S) Climate Data Store (CDS), https://doi.org/10.24381/cds.f17050d.

Hodges, K., A. Cobb, and P. L. Vidale, 2017: How Well Are Tropical Cyclones Represented in Reanalysis Datasets? *J. Climate*, **30 (14)**, 5243–5264, https://doi.org/10.1175/JCLI-D-16-0557.1.

Hodges, K. I., 1994: A general-method for tracking analysis and its application to meteorological data. *Mon. Wea. Rev.*, **122 (11)**, 2573–2586, https://doi.org/10.1175/1520-0493(1994)122⟨2573:AGMFTA⟩2.0.CO;2.

Hsieh, T.-L., G. A. Vecchi, W. Yang, I. M. Held, and S. T. Garner, 2020: Large-scale control on the frequency of tropical cyclones and seeds: a consistent relationship across a hierarchy of global atmospheric models. *Clim. Dyn.*, **55**, 3177–3196, https://doi.org/10.1007/s00382-020-05446-5.

Jing, R., and N. Lin, 2020: An Environment-Dependent Probabilistic Tropical Cyclone Model. *J. Adv. Model. Earth Sys.*, **12 (3)**, https://doi.org/10.1029/2019MS001975.

Judt, F., and Coauthors, 2021: Tropical Cyclones in Global Storm-Resolving Models. *J. Meteor. Soc. Japan*, **99 (3)**, 579–602, https://doi.org/10.2151/jmsj.2021-029.

Kelley, M., and Coauthors, 2020: GISS-E2.1: Configurations and Climatology. *J. Adv. Model. Earth Sys.*, **12 (8)**, e2019MS002 025, https://doi.org/10.1029/2019MS002025.

Knapp, K. R., H. J. Diamond, J. P. Kossin, M. C. Kruk, and C. J. Schreck III, 2018: International Best Track Archive for Climate Stewardship (IBTrACS) Project, Version 4. NOAA National Centers for Environmental Information, https://doi.org/10.25921/82TY-9E16.

Knapp, K. R., M. C. Kruk, D. H. Levinson, H. J. Diamond, and C. J. Neumann, 2010: The International Best Track Archive for Climate Stewardship (IBTrACS): Unifying Tropical Cyclone Data. *Bull. Amer. Meteor. Soc.*, **91 (3)**, 363–376, https://doi.org/10.1175/2009BAMS2755.1.

Knutson, T., and Coauthors, 2020: Tropical Cyclones and Climate Change Assessment: Part II: Projected Response to Anthropogenic Warming. *Bull. Amer. Meteor. Soc.*, **101 (3)**, E303–E322, https://doi.org/10.1175/BAMS-D-18-0194.1.

Knutson, T. R., J. J. Sirutis, M. A. Bender, R. E. Tuleya, and B. A. Schenkel, 2022: Dynamical downscaling projections of late twenty-first-century U.S. landfalling hurricane activity. *Climatic Change*, **171 (3)**, 28, https://doi.org/10.1007/s10584-022-03346-7.

Knutson, T. R., and Coauthors, 2010: Tropical cyclones and climate change. *Nature Geosci.*, **3 (3)**, 157–163, https://doi.org/10.1038/ngeo779.

Knutson, T. R., and Coauthors, 2013: Dynamical Downscaling Projections of Twenty-First-Century Atlantic Hurricane Activity: CMIP3 and CMIP5 Model-Based Scenarios. *J. Climate*, **26 (17)**, 6591–6617, https://doi.org/10.1175/JCLI-D-12-00539.1.

Kossin, J. P., 2017: Hurricane intensification along United States coast suppressed during active hurricane periods. *Nature*, **541 (7637)**, 390–393, https://doi.org/10.1038/nature20783.

Kossin, J. P., K. A. Emanuel, and S. J. Camargo, 2016: Past and Projected Changes in Western North Pacific Tropical Cyclone Exposure. *J. Climate*, **29 (16)**, 5725–5739, https://doi.org/10.1175/JCLI-D-16-0076.1.

Kossin, J. P., K. A. Emanuel, and G. A. Vecchi, 2014: The poleward migration of the location of tropical cyclone maximum intensity. *Nature*, **509 (7500)**, 349–352, https://doi.org/10.1038/nature13278.

Kruk, M. C., K. R. Knapp, and D. H. Levinson, 2010: A Technique for Combining Global Tropical Cyclone Best Track Data. *J. Atmos. Ocean. Tech.*, **27 (4)**, 680–692, https://doi.org/10.1175/2009JTECHA1267.1.

Kuhlbrodt, T., and Coauthors, 2018: The Low-Resolution Version of HadGEM3 GC3.1: Development and Evaluation for Global Climate. *J. Adv. Model. Earth Sys.*, **10 (11)**, 2865–2888, https://doi.org/10.1029/2018MS001370.

Landman, W. A., A. Seth, and S. J. Camargo, 2005: The Effect of Regional Climate Model Domain Choice on the Simulation of Tropical Cyclone–Like Vortices in the Southwestern Indian Ocean. *J. Climate*, **18 (8)**, 1263–1274, https://doi.org/10.1175/JCLI3324.1.

Lee, C.-Y., S. J. Camargo, A. H. Sobel, and M. K. Tippett, 2020a: Statistical–Dynamical Downscaling Projections of Tropical Cyclone Activity in a Warming Climate: Two Diverging Genesis Scenarios. *J. Climate*, **33 (11)**, 4815–4834, https://doi.org/10.1175/JCLI-D-19-0452.1.

Lee, C.-Y., A. H. Sobel, S. J. Camargo, M. K. Tippett, and Q. Yang, 2022: New York State Hurricane Hazard: History and Future Projections. *J. Appl. Meteor. Climatol.*, **61 (6)**, 613–629, https://doi.org/10.1175/JAMC-D-21-0173.1.

Lee, C.-Y., A. H. Sobel, M. K. Tippett, S. J. Camargo, M. Wüest, M. Wehner, and H. Murakami, 2023: Climate Change Signal in Atlantic Tropical Cyclones Today and Near Future. *Earth's Future*, **11 (11)**, e2023EF003 539, https://doi.org/10.1029/2023EF003539.

Lee, C.-Y., M. K. Tippett, A. H. Sobel, and S. J. Camargo, 2018: An Environmentally Forced Tropical Cyclone Hazard Model. *J. Adv. Model. Earth Sys.*, **10 (1)**, 223–241, https://doi.org/10.1002/2017MS001186.

Lee, J., J. Kim, M.-A. Sun, B.-H. Kim, H. Moon, H. M. Sung, J. Kim, and Y.-H. Byun, 2020b: Evaluation of the Korea Meteorological Administration Advanced Community Earth-System model (K-ACE). *Asia-Pacific J. Atmos. Sci.*, **56 (3)**, 381–395, https://doi.org/10.1007/s13143-019-00144-7.

Li, L., and Coauthors, 2020: The Flexible Global Ocean-Atmosphere-Land System Model Grid-Point Version 3 (FGOALS-g3): Description and Evaluation. *J. Adv. Model. Earth Sys.*, **12 (9)**, e2019MS002 012, https://doi.org/10.1029/2019MS002012.

Lin, I.-I., S. J. Camargo, C.-C. Lien, C.-A. Shi, and J. P. Kossin, 2023a: Poleward migration as global warming's possible self-regulator to restrain future western North Pacific Tropical Cyclone's intensification. *npj Clim. Atmos. Sci.*, **6 (1)**, 1–9, https://doi.org/10.1038/s41612-023-00329-y.

Lin, J., R. Rousseau-Rizzi, C.-Y. Lee, and A. Sobel, 2023b: An Open-Source, Physics-Based, Tropical Cyclone Downscaling Model With Intensity-Dependent Steering. *J. Adv. Model. Earth Sys.*, **15 (11)**, e2023MS003 686, https://doi.org/10.1029/2023MS003686.

Lin, Y., and Coauthors, 2020: Community Integrated Earth System Model (CIESM): Description and Evaluation. *J. Adv. Model. Earth Sys.*, **12 (8)**, e2019MS002 036, https://doi.org/10.1029/2019MS002036.

Lovato, T., and Coauthors, 2022: CMIP6 Simulations With the CMCC Earth System Model (CMCC-ESM2). *J. Adv. Model. Earth Sys.*, **14 (3)**, e2021MS002 814, https://doi.org/10.1029/2021MS002814.

Lund, M. T., G. Myhre, and B. H. Samset, 2019: Anthropogenic aerosol forcing under the Shared Socioeconomic Pathways. *Atmos. Chem. Phys.*, **19 (22)**, 13 827–13 839, https://doi.org/10.5194/acp-19-13827-2019.

Manganello, J. V., and Coauthors, 2012: Tropical Cyclone Climatology in a 10-km Global Atmospheric GCM: Toward Weather-Resolving Climate Modeling. *J. Climate*, **25 (11)**, 3867–3893, https://doi.org/10.1175/JCLI-D-11-00346.1.

Mauritsen, T., and Coauthors, 2019: Developments in the MPI-M Earth System Model version 1.2 (MPI-ESM1.2) and Its Response to Increasing CO2. *J. Adv. Model. Earth Sys.*, **11 (4)**, 998–1038, https://doi.org/10.1029/2018MS001400.

Miller, R. L., and Coauthors, 2021: CMIP6 Historical Simulations (1850–2014) With GISS-E2.1. *J. Adv. Model. Earth Sys.*, **13 (1)**, e2019MS002 034, https://doi.org/10.1029/2019MS002034.

Moon, Y., and Coauthors, 2020: Azimuthally Averaged Wind and Thermodynamic Structures of Tropical Cyclones in Global Climate Models and Their Sensitivity to Horizontal Resolution. *J. Climate*, **33 (4)**, 1575–1595, https://doi.org/10.1175/JCLI-D-19-0172.1.

Moon, Y., and Coauthors, 2022: An Evaluation of Tropical Cyclone Rainfall Structures in the HighResMIP Simulations against Satellite Observations. *J. Climate*, **35 (22)**, 3715–3738, https://doi.org/10.1175/JCLI-D-21-0564.1.

Murakami, H., and Coauthors, 2015: Simulation and Prediction of Category 4 and 5 Hurricanes in the High-Resolution GFDL HiFLOR Coupled Climate Model. *J. Climate*, **28 (23)**, 9058–9079, https://doi.org/10.1175/JCLI-D-15-0216.1.

Müller, W. A., and Coauthors, 2018: A Higher-resolution Version of the Max Planck Institute Earth System Model (MPI-ESM1.2-HR). *J. Adv. Model. Earth Sys.*, **10 (7)**, 1383–1413, https://doi.org/10.1029/2017MS001217.

Nakamura, J., U. Lall, Y. Kushnir, and B. Rajagopalan, 2015: HITS: Hurricane Intensity and Track Simulator with North Atlantic Ocean Applications for Risk Assessment. *J. Appl. Meteor. Climatol.*, **54 (7)**, 1620–1636, https://doi.org/10.1175/JAMC-D-14-0141.1.

Nijsse, F. J. M. M., P. M. Cox, and M. S. Williamson, 2020: Emergent constraints on transient climate response (TCR) and equilibrium climate sensitivity (ECS) from historical warming in CMIP5 and CMIP6 models. *Earth Syst. Dynam.*, **11 (3)**, 737–750, https://doi.org/10.5194/esd-11-737-2020.

O'Neill, B. C., and Coauthors, 2016: The Scenario Model Intercomparison Project (ScenarioMIP) for CMIP6. *Geosci. Model Dev.*, **9 (9)**, 3461–3482, https://doi.org/10.5194/gmd-9-3461-2016.

Pak, G., and Coauthors, 2021: Korea Institute of Ocean Science and Technology Earth System Model and Its Simulation Characteristics. *Ocean Sci. J.*, **56 (1)**, 18–45, https://doi.org/10.1007/s12601-021-00001-7.

Patricola, C. M., R. Saravanan, and P. Chang, 2014: The Impact of the El Niño–Southern Oscillation and Atlantic Meridional Mode on Seasonal Atlantic Tropical Cyclone Activity. *J. Climate*, **27 (14)**, 5311–5328, https://doi.org/10.1175/JCLI-D-13-00687.1.

Patricola, C. M., R. Saravanan, and P. Chang, 2017: A teleconnection between Atlantic sea surface temperature and eastern and central North Pacific tropical cyclones. *Geophys. Res. Lett.*, **44 (2)**, 1167–1174, https://doi.org/10.1002/2016GL071965.

Rao, S., and Coauthors, 2017: Future air pollution in the Shared Socio-economic Pathways. *Global Environ. Change*, **42**, 346–358, https://doi.org/10.1016/j.gloenvcha.2016.05.012.

Reed, K. A., J. T. Bacmeister, N. A. Rosenbloom, M. F. Wehner, S. C. Bates, P. H. Lauritzen, J. E. Truesdale, and C. Hannay, 2015: Impact of the dynamical core on the direct simulation of tropical cyclones in a high-resolution global model. *Geophys. Res. Lett.*, **42 (9)**, 3603–3608, https://doi.org/10.1002/2015GL063974.

Rios-Berrios, R., P. M. Finocchio, J. J. Alland, X. Chen, M. S. Fischer, S. N. Stevenson, and D. Tao, 2023: A Review of the Interactions between Tropical Cyclones and Environmental Vertical Wind Shear. *J. Atmos. Sci.*, **81 (4)**, 713–741, https://doi.org/10.1175/JAS-D-23-0022.1.

Roberts, M. J., and Coauthors, 2015: Tropical Cyclones in the UPSCALE Ensemble of High-Resolution Global Climate Models. *J. Climate*, **28 (2)**, 574–596, https://doi.org/10.1175/JCLI-D-14-00131.1.

Roberts, M. J., and Coauthors, 2020a: Impact of Model Resolution on Tropical Cyclone Simulation Using the HighResMIP–PRIMAVERA Multimodel Ensemble. *J. Climate*, **33 (7)**, 2557–2583, https://doi.org/10.1175/JCLI-D-19-0639.1.

Roberts, M. J., and Coauthors, 2020b: Projected Future Changes in Tropical Cyclones Using the CMIP6 HighResMIP Multimodel Ensemble. *Geophys. Res. Lett.*, **47 (14)**, e202GL088 662, https://doi.org/10.1029/2020GL088662.

Rong, X., J. Li, H. Chen, J. Su, L. Hua, Z. Zhang, and Y. Xin, 2021: The CMIP6 Historical Simulation Datasets Produced by the Climate System Model CAMS-CSM. *Adv. Atmos. Sci.*, **38 (2)**, 285–295, https://doi.org/10.1007/s00376-020-0171-y.

Rong, X., and Coauthors, 2018: The CAMS Climate System Model and a Basic Evaluation of Its Climatology and Climate Variability Simulation. *J Meteorol Res*, **32 (6)**, 839–861, https://doi.org/10.1007/s13351-018-8058-x.

Russotto, R. D., and Coauthors, 2022: Evolution of Tropical Cyclone Properties Across the Development Cycle of the GISS-E3 Global Climate Model. *J. Adv. Model. Earth Sys.*, **14 (1)**, e2021MS002 601, https://doi.org/10.1029/2021MS002601.

Schreck, C. J., K. R. Knapp, and J. P. Kossin, 2014: The Impact of Best Track Discrepancies on Global Tropical Cyclone Climatologies using IBTrACS. *Mon. Wea. Rev.*, **142 (10)**, 3881–3899, https://doi.org/10.1175/MWR-D-14-00021.1.

Schär, C., and Coauthors, 2020: Kilometer-Scale Climate Models: Prospects and Challenges. *Bull. Amer. Meteor. Soc.*, https://doi.org/10.1175/BAMS-D-18-0167.1.

Seager, R., M. Cane, N. Henderson, D.-E. Lee, R. Abernathey, and H. Zhang, 2019: Strengthening tropical Pacific zonal sea surface temperature gradient consistent with rising greenhouse gases. *Nat. Clim. Change*, **9 (7)**, 517–522, https://doi.org/10.1038/s41558-019-0505-x.

Seland, Ø., and Coauthors, 2020: Overview of the Norwegian Earth System Model (NorESM2) and key climate response of CMIP6 DECK, historical, and scenario simulations. *Geosci. Model. Dev.*, **13 (12)**, 6165–6200, https://doi.org/10.5194/gmd-13-6165-2020.

Sellar, A. A., and Coauthors, 2019: UKESM1: Description and Evaluation of the U.K. Earth System Model. *J. Adv. Model. Earth Sys.*, **11 (12)**, 4513–4558, https://doi.org/10.1029/2019MS001739.

Semmler, T., and Coauthors, 2020: Simulations for CMIP6 With the AWI Climate Model AWI-CM-1-1. *J. Adv. Model. Earth Sys.*, **12 (9)**, e2019MS002 009, https://doi.org/10.1029/2019MS002009.

Seneviratne, S. I., and M. Hauser, 2020: Regional Climate Sensitivity of Climate Extremes in CMIP6 Versus CMIP5 Multimodel Ensembles. *Earth's Future*, **8 (9)**, https://doi.org/10.1029/2019EF001474.

Shaevitz, D. A., and Coauthors, 2014: Characteristics of tropical cyclones in high-resolution models in the present climate. *J. Adv. Model. Earth Sys.*, **6 (4)**, 1154–1172, https://doi.org/10.1002/2014MS000372.

Sobel, A. H., S. J. Camargo, T. M. Hall, C.-Y. Lee, M. K. Tippett, and A. A. Wing, 2016: Human influence on tropical cyclone intensity. *Science*, **353 (6296)**, 242–246, https://doi.org/10.1126/science.aaf6574.

Sobel, A. H., S. J. Camargo, and M. Previdi, 2019: Aerosol versus Greenhouse Gas Effects on Tropical Cyclone Potential Intensity and the Hydrologic Cycle. *J. Climate*, **32 (17)**, 5511–5527, https://doi.org/10.1175/JCLI-D-18-0357.1.

Sobel, A. H., A. A. Wing, S. J. Camargo, C. M. Patricola, G. A. Vecchi, C.-Y. Lee, and M. K. Tippett, 2021: Tropical Cyclone Frequency. *Earth's Future*, **9 (12)**, e2021EF002 275, https://doi.org/10.1029/2021EF002275.

Sobel, A. H., and Coauthors, 2023: Near-term tropical cyclone risk and coupled Earth system model biases. *Proc. Natl. Acad. Sci. USA*, **120 (33)**, e2209631 120, https://doi.org/10.1073/pnas.2209631120.

Stansfield, A. M., K. A. Reed, and C. M. Zarzycki, 2020: Changes in Precipitation From North Atlantic Tropical Cyclones Under RCP Scenarios in the Variable-Resolution Community Atmosphere Model. *Geophys. Res. Lett.*, **47 (12)**, e2019GL086 930, https://doi.org/10.1029/2019GL086930.

Swart, N. C., and Coauthors, 2019: The Canadian Earth System Model version 5 (CanESM5.0.3). *Geosci. Model. Dev.*, **12 (11)**, 4823–4873, https://doi.org/10.5194/gmd-12-4823-2019.

Séférian, R., and Coauthors, 2019: Evaluation of CNRM Earth System Model, CNRM-ESM2-1: Role of Earth System Processes in Present-Day and Future Climate. *J. Adv. Model. Earth Sys.*, **11 (12)**, 4182–4227, https://doi.org/10.1029/2019MS001791.

Tang, B., and S. J. Camargo, 2014: Environmental control of tropical cyclones in CMIP5: A ventilation perspective. *J. Adv. Model. Earth Sys.*, **6 (1)**, 115–128, https://doi.org/10.1002/2013MS000294.

Tang, B., and K. Emanuel, 2010: Midlevel Ventilation's Constraint on Tropical Cyclone Intensity. *J. Atmos. Sci.*, **67 (6)**, 1817–1830, https://doi.org/10.1175/2010JAS3318.1.

Tang, B., and K. Emanuel, 2012: A Ventilation Index for Tropical Cyclones. *Bull. Amer. Meteor. Soc.*, **93 (12)**, 1901–1912, https://doi.org/10.1175/BAMS-D-11-00165.1.

Tatebe, H., and Coauthors, 2019: Description and basic evaluation of simulated mean state, internal variability, and climate sensitivity in MIROC6. *Geosci. Model. Dev.*, **12 (7)**, 2727–2765, https://doi.org/10.5194/gmd-12-2727-2019.

Taylor, K. E., 2001: Summarizing multiple aspects of model performance in a single diag ram. *J. Geophys. Res.*, **106 (D7)**, 7183–7192, https://doi.org/10.1029/2000JD900719.

Ting, M., S. J. Camargo, C. Li, and Y. Kushnir, 2015: Natural and Forced North Atlantic Hurricane Potential Intensity Change in CMIP5 Models. *J. Climate*, **28 (10)**, 3926–3942, https://doi.org/10.1175/JCLI-D-14-00520.1.

Ting, M., J. P. Kossin, S. J. Camargo, and C. Li, 2019: Past and Future Hurricane Intensity Change along the U.S. East Coast. *Sci. Rep.*, **9 (1)**, 7795, https://doi.org/10.1038/s41598-019-44252-w.

Tippett, M. K., S. J. Camargo, and A. H. Sobel, 2011: A Poisson Regression Index for Tropical Cyclone Genesis and the Role of Large-Scale Vorticity in Genesis. *J. Climate*, **24 (9)**, 2335–2357, https://doi.org/10.1175/2010JCLI3811.1.

Tory, K. J., S. S. Chand, J. L. McBride, H. Ye, and R. A. Dare, 2013: Projected Changes in Late-Twenty-First-Century Tropical Cyclone Frequency in 13 Coupled Climate Models from Phase 5 of the Coupled Model Intercomparison Project. *J. Climate*, **26 (24)**, 9946–9959, https://doi.org/10.1175/JCLI-D-13-00010.1.

Vecchi, G. A., S. Fueglistaler, I. M. Held, T. R. Knutson, and M. Zhao, 2013: Impacts of Atmospheric Temperature Trends on Tropical Cyclone Activity. *J. Climate*, **26 (11)**, 3877–3891, https://doi.org/10.1175/JCLI-D-12-00503.1.

Vecchi, G. A., and B. J. Soden, 2007a: Effect of remote sea surface temperature change on tropical cyclone potential intensity. *Nature*, **450 (7172)**, 1066–1070, https://doi.org/10.1038/nature06423.

Vecchi, G. A., and B. J. Soden, 2007b: Increased tropical Atlantic wind shear in model projections of global warming. *Geophys. Res. Lett.*, **34 (8)**, L08 702, https://doi.org/10.1029/2006GL028905.

Vickery, P. J., 2005: Simple Empirical Models for Estimating the Increase in the Central Pressure of Tropical Cyclones after Landfall along the Coastline of the United States. *J. Appl. Meteorol.*, **44 (12)**, 1807–1826, https://doi.org/10.1175/JAM2310.1.

Vidale, P. L., and Coauthors, 2021: Impact of Stochastic Physics and Model Resolution on the Simulation of Tropical Cyclones in Climate GCMs. *J. Climate*, **34 (11)**, 4315–4341, https://doi.org/10.1175/JCLI-D-20-0507.1.

Voldoire, A., and Coauthors, 2019: Evaluation of CMIP6 DECK Experiments With CNRM-CM6-1. *J. Adv. Model. Earth Sys.*, **11 (7)**, 2177–2213, https://doi.org/10.1029/2019MS001683.

Volodin, E. M., N. A. Dianskii, and A. V. Gusev, 2010: Simulating present-day climate with the INMCM4.0 coupled model of the atmospheric and oceanic general circulations. *Izv. Atmos. Ocean. Phys.*, **46 (4)**, 414–431, https://doi.org/10.1134/S000143381004002X.

Volodin, E. M., and Coauthors, 2017: Simulation of the present-day climate with the climate model INMCM5. *Clim Dyn*, **49 (11)**, 3715–3734, https://doi.org/10.1007/s00382-017-3539-7.

Wang, Y.-C., and Coauthors, 2021: Performance of the Taiwan Earth System Model in Simulating Climate Variability Compared With Observations and CMIP6 Model Simulations. *J. Adv. Model. Earth Sys.*, **13 (7)**, e2020MS002 353, https://doi.org/10.1029/2020MS002353.

Wehner, M., Prabhat, K. A. Reed, D. Stone, W. D. Collins, and J. Bacmeister, 2015: Resolution Dependence of Future Tropical Cyclone Projections of CAM5.1 in the U.S. CLIVAR Hurricane Working Group Idealized Configurations. *J. Climate*, **28 (10)**, 3905–3925, https://doi.org/10.1175/JCLI-D-14-00311.1.

Wehner, M. F., and J. P. Kossin, 2024: The growing inadequacy of an open-ended Saffir–Simpson hurricane wind scale in a warming world. *Proc. Natl. Acad. Sci. USA*, **121 (7)**, e2308901 121, https://doi.org/10.1073/pnas.2308901121.

Wehner, M. F., and Coauthors, 2014: The effect of horizontal resolution on simulation quality in the Community Atmospheric Model, CAM5.1. *J. Adv. Model. Earth Sys.*, **6 (4)**, 980–997, https://doi.org/10.1002/2013MS000276.

Wing, A. A., K. Emanuel, and S. Solomon, 2015: On the factors affecting trends and variability in tropical cyclone potential intensity. *Geophys. Res. Lett.*, **42 (20)**, 8669–8677, https://doi.org/10.1002/2015GL066145.

Wing, A. A., A. H. Sobel, and S. J. Camargo, 2007: The Relationship Between the Potential and Actual Intensities of Tropical Cyclones. *Geophys. Res. Lett.*, **34 (8)**, L08 810, https://doi.org/10.1029/2006GL028581.

Wu, T., and Coauthors, 2019: The Beijing Climate Center Climate System Model (BCC-CSM): the main progress from CMIP5 to CMIP6. *Geosci. Model. Dev.*, **12 (4)**, 1573–1600, https://doi.org/10.5194/gmd-12-1573-2019.

Xu, W., K. Balaguru, D. R. Judi, J. Rice, L. R. Leung, and S. Lipari, 2024: A North Atlantic synthetic tropical cyclone track, intensity, and rainfall dataset. *Sci. Data*, **11 (1)**, 130, https://doi.org/10.1038/s41597-024-02952-7.

Yukimoto, S., and Coauthors, 2019: The Meteorological Research Institute Earth System Model Version 2.0, MRI-ESM2.0: Description and Basic Evaluation of the Physical Component. *J. Meteor. Soc. Japan*, **97 (5)**, 931–965, https://doi.org/10.2151/jmsj.2019-051.

Zarzycki, C. M., C. Jablonowski, and M. A. Taylor, 2014: Using Variable-Resolution Meshes to Model Tropical Cyclones in the Community Atmosphere Model. *Mon. Wea. Rev.*, **142 (3)**, 1221–1239, https://doi.org/10.1175/MWR-D-13-00179.1.

Zelinka, M. D., T. A. Myers, D. T. McCoy, S. Po-Chedley, P. M. Caldwell, P. Ceppi, S. A. Klein, and K. E. Taylor, 2020: Causes of Higher Climate Sensitivity in CMIP6 Models. *Geophys. Res. Lett.*, **47 (1)**, https://doi.org/10.1029/2019GL085782.

Zhang, H., and Coauthors, 2020: Description and Climate Simulation Performance of CAS-ESM Version 2. *J. Adv. Model. Earth Sys.*, **12 (12)**, e2020MS002 210, https://doi.org/10.1029/2020MS002210.

Zhao, M., and I. M. Held, 2012: TC-Permitting GCM Simulations of Hurricane Frequency Response to Sea Surface Temperature Anomalies Projected for the Late-Twenty-First Century. *J. Climate*, **25 (8)**, 2995–3009, https://doi.org/10.1175/JCLI-D-11-00313.1.

Zick, S. E., and C. J. Matyas, 2015: Tropical cyclones in the North American Regional Reanalysis: An assessment of spatial biases in location, intensity, and structure. *J. Geophys. Res.*, **120 (5)**, 1651–1669, https://doi.org/10.1002/2014JD022417.

Ziehn, T., and Coauthors, 2020: The Australian Earth System Model: ACCESS-ESM1.5. *J. South. Hemisphere Earth Sys. Sci.*, **70 (1)**, 193–214, https://doi.org/10.1071/ES19035.